Matter and Radiation at Extremes REVIEW scitation.org/journal/mre

Synchrotron-based infrared microspectroscopy under high pressure: An introduction

Cite as: Matter Radiat. Extremes 6, 068202 (2021); doi: 10.1063/5.0071856
Submitted: 17 September 2021 • Accepted: 21 October 2021 •
Published Online: 12 November 2021

Lingping Kong[a] and Gang Liu

AFFILIATIONS

Center for High Pressure Science and Technology Advanced Research, Shanghai 201203, China

Note: This paper is a part of the Special Topic Collection on High Pressure Science 2021.
[a]**Author to whom correspondence should be addressed:** konglp@hpstar.ac.cn

ABSTRACT

Synchrotron sources with high photon flux, small source size, and broad energy range have revolutionized ultrafine characterization of condensed matter. With the addition of the pressure dimension realized by the use of diamond anvil cells, enormous progress has been achieved throughout high-pressure science. This is particularly so for synchrotron-based infrared microspectroscopy (SIRMS) with its very high signal-to-noise ratio, high spatial resolution, and extended measurement conditions. SIRMS has high sensitivity, providing a platform for the investigations of the very small amounts of material that need to be used in high-pressure research. This review summarizes developments in SIRMS, focusing on instrumentation and high-pressure measurements. Applications to measurements of infrared reflectance and absorption are presented, illustrating how SIRMS results play a crucial role in advancing understanding of the crystalline phase transitions, electronic transitions, metallization, lattice dynamics, superconductivity, and novel functional behavior. New insights into spectroscopic properties, together with some cutting edge issues and open problems, are also briefly discussed.

I. BACKGROUND

Arising from the nature of light–matter interaction, infrared spectroscopy (IRS) can detect the motions of molecular bonds, such as vibration and rotation, upon absorption of IR light. Molecular motions can range from the simple coupled motion of the two atoms of a diatomic molecule to the much more complex motion of each atom in a large molecule.[1] In principle, every molecule has its own interaction with a broadband IR source and vibrational modes that differ slightly from those of all other molecules, and thus the profile obtained from IRS can be viewed as a *fingerprint* providing unique information related to a molecule's structure and properties.[2] Consequently, IRS has been employed to identify various molecules and chemical bonds, and is employed in a wide range of research fields, including physics, chemistry, materials science, geosciences, and biosciences.[3–12] IRS also provides a powerful tool to examine the electrodynamics of solids.[2] For some solids, such as superconductors, that represent strongly correlated electron systems, the crucial physical properties are mainly determined by their electronic structures near the Fermi level, i.e., the energy level in the energy band diagram for which the probability of occupancy is 50% at nonzero temperature. Since the energy scale of photons from IR radiation (of the order of 10^{-4} to 1 eV) corresponds to the temperatures (of the order of $1–10^4$ K) at which electrodynamics-dominated properties emerge, many phenomena, such as low-energy excitations, metallization, superconducting gaps, charge density waves, Mott transitions, bandgap transitions, and carrier dynamics, have been investigated using IRS.[4,8,13–20] Furthermore, many factors, including temperature, humidity, pressure, the properties of the material sample being studied (size, thickness, doping, etc.), and measurement conditions, can affect IRS results.[21–26] Figure 1 shows various ranges of the IR spectrum, namely, namely far-IR, mid-IR, and near-IR, together with some important phenomena that can be studied by IRS.[2]

Synchrotrons are facilities in which a particle beam is accelerated and travels around a storage ring, providing electromagnetic radiation with wavelengths ranging from IR to x-rays.[27–29] It should be noted that IR and x-ray synchrotron radiation differ in some important respects. Synchrotron x-ray beams exhibit both extremely high flux and high brilliance, whereas synchrotron IR beams do not have high fluxes compared with standard sources. Here, for a light source, the flux Φ and brilliance B are defined respectively as

$$\Phi = \frac{n_{\mathrm{ph}}}{\Delta t \cdot 0.1\%\mathrm{BW}} \quad (1)$$

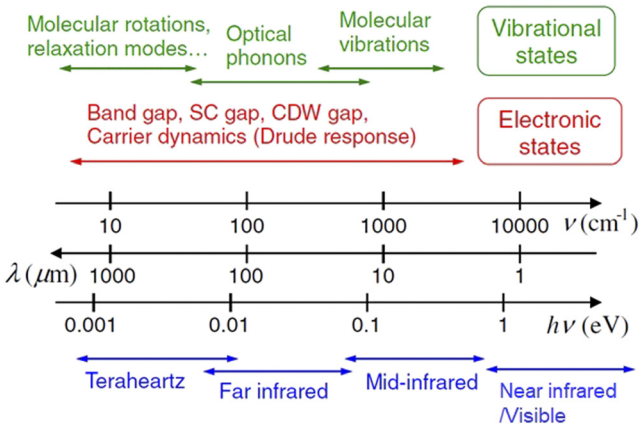

FIG. 1. Ranges of IR spectroscopy and the characteristic frequencies of various phenomena. Reprinted with permission from Okamura *et al.*, Jpn. J. Appl. Phys., Part 1 **56**(5S3), 05FA11 (2017). Copyright 2017 IOP Publishing.

and

$$B = \frac{n_{\mathrm{ph}}}{\Delta t \cdot \varepsilon_x \cdot \varepsilon_y \cdot 0.1\%\mathrm{BW}}. \quad (2)$$

Both flux and brilliance take spectral purity into account, since they measure the number of photons per second ($n_{\mathrm{ph}}/\Delta t$) in a 0.1% bandwidth (BW), where the presence of the term BW emphasizes that the flux, brilliance, and power are frequency-dependent quantities. The properties of a synchrotron light source are also strongly dependent on its size and angular distribution, and this is represented by the presence of the emittances in the horizontal and vertical directions, ε_x and ε_y, respectively, in the expression for the brilliance. It can therefore be seen that a small emittance is desirable for a high-brilliance radiation source and that the source quality is superior if all the photons travel in the same direction.

The first IR beamline installation was that at Daresbury in the UK in the 1980s, and since then many have been constructed, commissioned, and put into use worldwide, indeed at almost every third-generation light source.[30,31] Synchrotron sources have a brilliance advantage of 100–1000 times compared with blackbody sources (conventional thermal Globar sources), enabling IR synchrotron radiation to achieve very high signal-to-noise ratios. In addition, the small divergence angle of synchrotron radiation provides an opportunity to achieve diffraction-limited spatial resolution, making it promising for microspectroscopic studies on individual sample spots at the microscale.[28] In addition, their ultrahigh brilliance enables synchrotron light sources to be continuum sources with spectral coverage from the far-IR to x-rays, which is crucial for research on picosecond-level pump–probe dynamics, where varying photon wavelengths are required.[27]

With the development of diamond anvil cell (DAC) techniques, high-pressure research is emerging as a new dimension in a wide variety of scientific fields. With the addition of the pressure dimension, we can still use electromagnetic radiation to characterize samples at megabar pressures, significantly contributing to reliable exploration of structure–property relationship. Pressure can be viewed as a control knob by which the crystal lattice and electronic wave functions can be continuously modulated.[2,29] In this context, the strengths of some molecular interactions can be varied by several orders of magnitude and the frequency of vibrations can be abruptly changed while monitoring IR response is monitored. Pressure is also believed to be an effective post-synthesis method for improving material performance, and thus *in situ* spectroscopic studies are a critical requirement for exploring the underlying mechanism with further development in materials engineering in mind.[32] Compared with its in-laboratory IR counterpart, synchrotron-based infrared microspectroscopy (SIRMS) is particularly suitable for high-pressure studies (even more so for ultrahigh-pressure cases), because the beam spot of the IR synchrotron radiation can be focused tightly on a sample and its size is a good match with the diameter of the gasket hole in a DAC.

In this paper, the SIRMS technique for high-pressure research is briefly introduced. We first review the facilities that are available worldwide, with an emphasis on the crucial performance aspects of IR beamlines. We also discuss the combination of the DAC technique and SIRMS. Then, considering the latest research progress, we illustrate how SIRMS has been employed in high-pressure science and why it plays such an important role in advancing our understanding of high-pressure phenomena.

II. FACILITIES

A. Light source, beam splitter, and detector

In this section, we will introduce the SIRMS facilities in outline. For an IR system, the light source is a fundamental component and directly affects the sensitivity and quality of measurements. Currently, high-pressure mercury lamps, resistively heated silicon carbide rods (known as Globars), and tungsten-filament light bulbs or quartz–tungsten–halogen (QTH) lamps, are the most common light sources for far-, mid-, and near-IR, respectively.[1] There is increasing interest in extending the spectral range covered from near-IR frequencies down to even the terahertz (THz) region. In this context, synchrotron radiation is particularly suitable as a bright source for measurements requiring higher brilliance and/or higher intensity in the far-IR region.

Conventionally, in a synchrotron-based IR beamline, the IR radiation is generated as electrons pass through the spatially uniform magnetic field in the central region of a bending magnet (BM) of the electron storage ring.[33] Recently, however, the so-called edge radiation (ER) generated by electrons as they pass through the rapidly spatially varying magnetic fields in the edge regions at the entrance and exit of a BM has been considered for use as a bright IR source.[34,35] Calculations have shown that although the fluxes of BM- and ER-generated emissions are almost the same in magnitude, there are significant differences in intensity distribution and polarization properties between the two types of emission, because the opening angle of the ER emission is narrower than that of the BM type.[36,37] It should also be noted that although the flux or brilliance of a synchrotron light source can be high, it does not always generate much higher power than an in-laboratory facility, but, owing to diffraction-limited performance, it provides a much higher flux for a single spot of size of the order of a micrometer.[27] The spot size of a synchrotron-based IR beam is determined by both the diffraction-limit factor d_{R} and the transverse synchrotron electron beam size σ as follows:

$$\text{spot size} = m\left[(d_R\lambda)^{1/2} + \sigma^{1/2}\right]^{1/2}, \quad (3)$$

where m and λ are the overall demagnification factor and the wavelength of the light, respectively. As the wavelength of a synchrotron light is usually very short, σ is the dominant factor, and this is affected by the operating conditions as well as the energy spread of a given storage ring.[28]

Figure 2 compares the dependence of the integrated intensity of the IR spectrum on the aperture size of the microscope between facilities using a Globar and a synchrotron light source, respectively.[38] With a Globar, the intensity within the aperture area decreases as the aperture size decreases, whereas, with a synchrotron light source, the intensity of the synchrotron radiation maintains a maximum level when the aperture size is larger than $30 \times 30\ \mu m^2$. Therefore, owing to the small beam size, the whole beam spot is able to pass through the aperture. This feature is particularly desirable for high-pressure studies, where the sample size is of the same order of magnitude as the beam size. In addition to its small beam size, synchrotron radiation also exhibits a high degree of linear polarization in the orbital plane of the electron beam and circular polarization out of this plane, and thus both linear and circular dichroism experiments are feasible.

Besides the light source, the beam splitter and detector are also of vital importance to the successful operation of most Fourier transform IR (FT-IR) spectrometers. An IR beam splitter is designed to simultaneously transmit and reflect 50% of the incident beam between two optical elements. Beam splitters are usually made from high-grade glass materials with high-damage-threshold coatings, which allow them to survive under high-power laser energy.[1] Additional requirements include laser-grade surface flatness and surface quality, and a tight tolerance on the splitting ratio. Common beam splitters used for IRS are listed in Table I, from which it can be seen that various IR plate beam splitters with different coatings have been designed for different spectral ranges. For example, a broadband KBr beam splitter can cover both the mid- and near-IR spectral ranges from 10 000 to 385 cm^{-1} (note that the detectors and sources need to be selected appropriately for optimal performance). Alternatively, Mylar-type beam splitters are designed for use in the far-IR range. In addition to the spectral range, the design of the beam splitter also needs to consider other factors, such as dimensions, desired substrate, incident beam angle, requirements on durability, thermal shock resistance, and low absorption, convenient mounting in standard optical mirror mounts, and stability requirements for both the splitter itself and the whole system.[1]

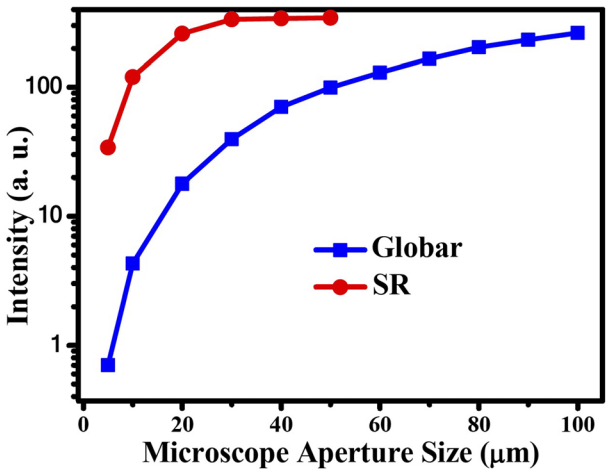

FIG. 2. Dependence of IR intensity on microscope aperture size for Globar and synchrotron sources at the Hefei Light Source, National Synchrotron Radiation Laboratory, China. The beam current is 360 mA. The spectra were collected in the mid-IR range of 600–4000 cm^{-1}. Reprinted with permission from Hu *et al.*, Infrared Phys. Technol. **105**, 103200 (2020). Copyright 2020 Elsevier B.V.

TABLE I. Various beam splitters covering different spectral ranges.

Beam splitter	Spectral range (cm^{-1})
KBr (broadband)	10 000–380
CaF_2-NIR	15 500–1200
Quartz-VIS	25 000–8000
Quartz-UV/VIS/NIR	55 000–4000
Mylar 23 μm-FAR	120–30
Mylar 50 μm-FAR	60–8
Mylar 125 μm-FAR	25–5

There are two types of IR detectors, namely, thermal detectors and photonic detectors, with the former being based on temperature-dependent phenomena such as changes in resistance, the thermoelectric effect, and the thermal expansion effect, while the latter employ narrow-bandgap semiconductors with a p–n junction at which a photoelectric current appears upon illumination and need to be used at low temperature condition to reduce thermal noise.[1] The crucial performance parameters for an IR detector are sensitivity (detectivity), signal-to-noise ratio, and response time. Sometimes the nature of the electronic structure of a given material means that a compromise must be made between sensitivity, sensible spectra range, and cost. There is no single type of detector covering the whole IR spectrum, and so various different types of detector have been developed. Mercury–cadmium–telluride (abbreviated MCT) detectors are used in mid-IR, where it is possible to tune the material to sense longer or shorter wavelengths by varying the ratio of mercury to cadmium to telluride. In this context, three types of MCT detectors, MCT A/B/C, are employed, where MCT/A is a narrowband detector for the 8000–650 cm^{-1} range with high sensitivity, low noise, and quick response time, while MCT/B and MCT/C are broadband detectors for 10 000–400 and 10 000 to 580 cm^{-1}, respectively, but with lower sensitivity. For near-IR, InGaAs- and InSb-based detectors are employed, while DLATGS and Si bolometers are used for far-IR. Figure 3 shows the detectivities of various detectors and demonstrates the strong frequency dependence of each type of detector.

Other core components of a SIRMS station include an IR microscope and spectrometer, which are mature products that are widely available commercially and therefore will not be discussed here in detail.

B. Beamline

Since the first IR beamline installation appeared in the 1980s, SIRMS stations have been successfully developed at most of synchrotron

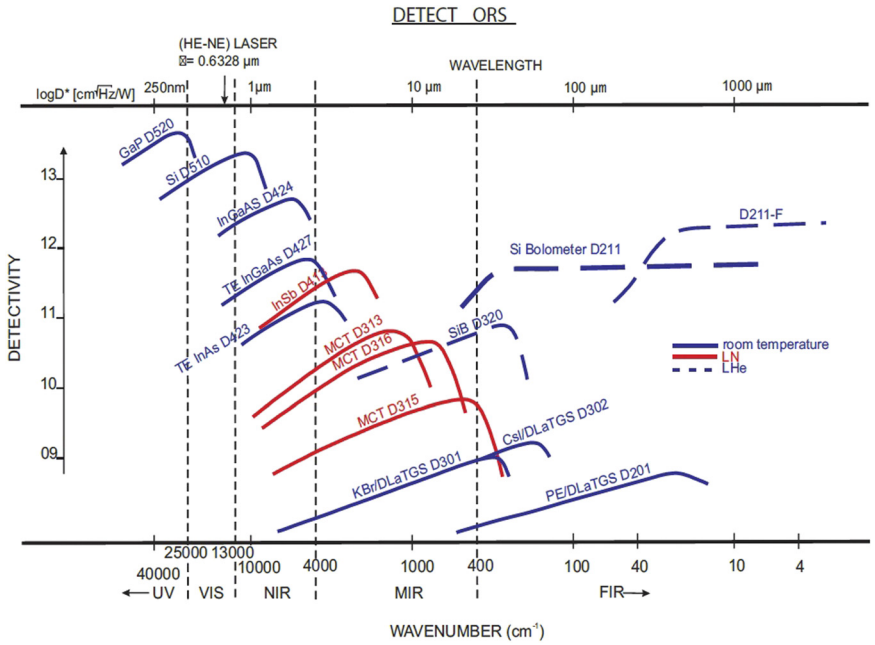

FIG. 3. Performance of various detectors. Reprinted from dataset of Bruker Corporation, "Application Note AN M161." Copyright 2019 Author(s).[39]

light sources worldwide, as listed in Table II,[27,30,31,38,40–52] from which we note that some sources such as SSRF and Soleil even have more than one SIRMS station. By integrating microscope optics and a sample stage, these beamlines enable high-pressure measurements of the reflectance spectrum and transmission spectrum of a sample contained in a DAC. Samples in a DAC assembled to reach pressures in excess of 100 GPa have dimensions of a few tens of micrometers, which is close to the diffraction limit for mid-IR. For such DAC-associated IR experiments on samples with small size, brilliance is a figure of merit that is even more important than flux. Owing to its smaller solid angle cone, the emission from ER usually has a higher brilliance than the classic dipole emission based on BM radiation over most of the IR spectral range, and thus it has been employed in some third-generation light sources.[31]

TABLE II. Parameters of IR beamlines worldwide.

Synchrotron	Beamline	E (GeV)	I (mA)	Collection angles (H × V, mrad)	IR source[a]	Spectral range (cm^{-1})	Temperature range[b]	Year
ALS (USA)	1.4.	1.4	500	40 × 10	BM	200–11 000	7–400 K (development)	1997
SPring-8 (Japan)	BL43IR	8	100	36.5 × 12.6	BM	100–8 000	4.2–400 K/83–873 K	2001
Bessy II (Germany)	IRIS	1.9	100	60 × 30	BM	30–20 000	1.6–500 K	2001
ELETTRA (Italy)	BL9.1	2–2.4	150–320	65 × 25	BM	100–visible	80 K–RT	2004
Australian (AS)	IR	3	200	58 × 17	ER+BM	THz–visible	⋯	2006
CLS (Canada)	Mid-IR Far-IR	2.9	300	55 × 37	BM	560–6 000 5–1 000	RT	2006
SOLEIL (France)	SMIS AILES	2.75	500	78 × 20	ER+BM	10–8 000	5 K–RT	2006
Diamond (UK)	B22	3	500	55 × 30	ER+BM	5–10 000	77–873 K	2007
SESAME (Jordan)	IR	2.5	400	39 × 15	ER+BM	50–12 500	RT	2012
SSRF (China)	BL01B	3.5	300	40 × 20	ER	600–10 000	4.2 K–RT	2013
PAL (Korea)	12D IRS	2.5–3.0	400	66 × 18	ER+BM	200–7 000	RT	2016
ALBA (Spain)	BL01	3	400	43 × 25.17	ER+BM	100–10 000	RT	2016
HLSII (China)	U4	0.8	360	60 × 55	BM	20–8 000	5–500	2016
SSRF (China)	BL06B	3.5	300	40 × 20	ER	10–12 800	4.2 K–RT	2020

[a]BM, bending magnets; ER, edge radiation.
[b]RT, room temperature.

Spectral range and system stability are two other crucial performance indicators. Although a white spectrum with all wavelengths present is available from a synchrotron light source, to obtain a continuous spectrum for an IR beamline, it is necessary to eliminate absorption and diffraction by the environment and from optical elements. Absorption by atmospheric gases such as water vapor and carbon dioxide can lead to a significantly decreased sample signal in mid- and far-IR spectroscopy, and thus to an inferior signal-to-noise ratio because less light reaches the detector, and meanwhile the concentration of these gases will accumulate with time. Therefore, a high vacuum is of vital importance, which is usually achieved by a special optical design. In addition, ultrahigh stability of the beam is essential for SIRMS experiments, since shifts in beam position and/or intensity can lead to indeterminacy or even errors in obtaining the IR spectrum via Fourier transform, especially for those experiments requiring a long data collection time. For each light source, particular parameters are optimized to deal with the stability issue, with both optical and thermal stability issues being taken into account.

It is not possible to discuss all the SIRMS stations here, and in any case some beamlines have been reviewed elsewhere. Instead we briefly introduce a station dedicated to high-pressure studies, namely, that located at beamline BL01B of the Shanghai Synchrotron Radiation Facility.[53] This beamline collects both ER and BM emissions that are suitable for mid-IR and near-IR studies. The collimated synchrotron beam is directed into the entrance port of a Nicolet 8700 FT-IR spectrometer with KBr and CaF_2 beam splitters, and it is then divided to match with a custom-built IR microscope system. This system is designed for ultrahigh-pressure projects, combining SIRMS with broadband laser visible/near-IR and conventional laser Raman spectroscopy in one instrument. The integrated Raman spectroscopy is

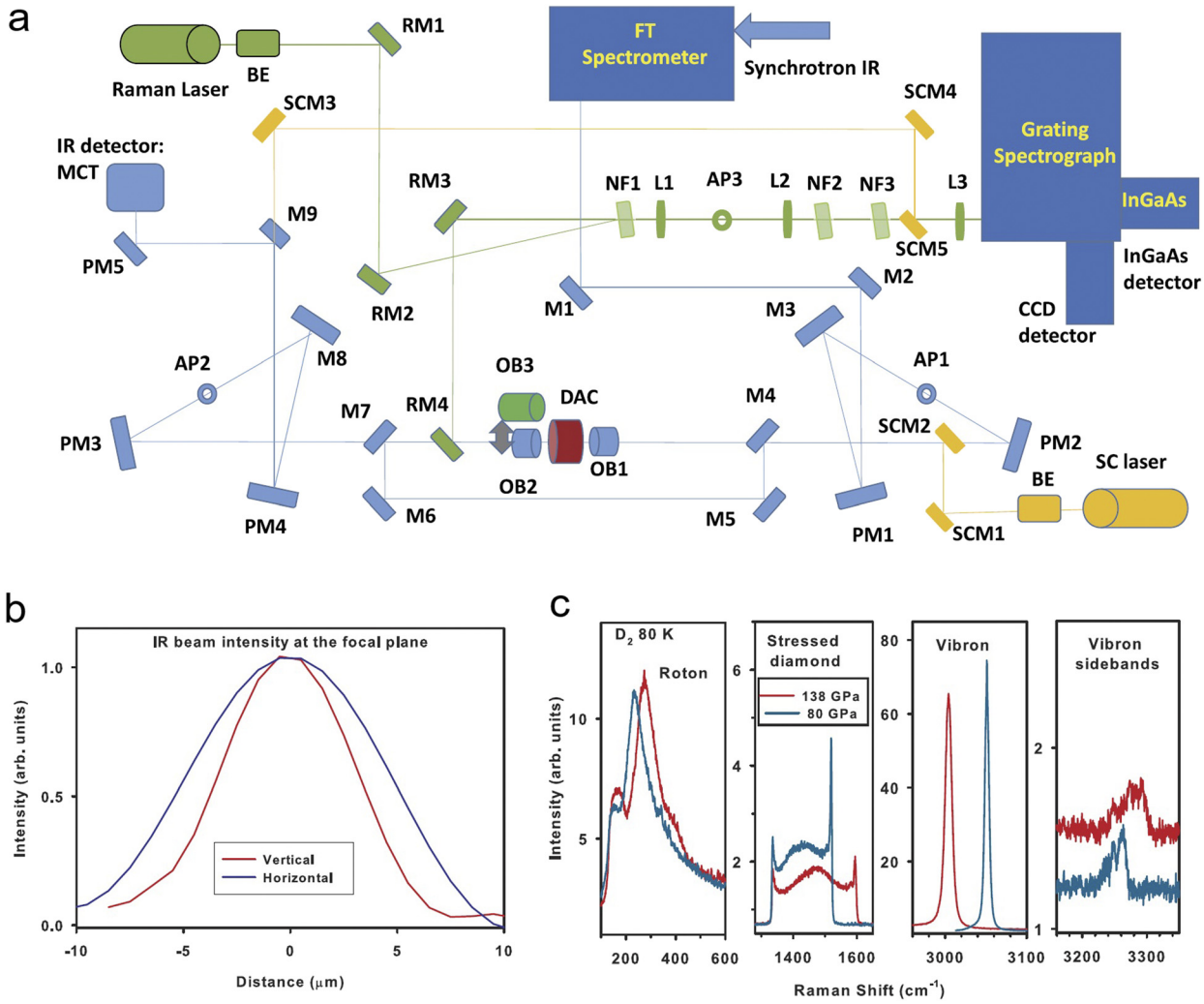

FIG. 4. Design and performance of the high-pressure SIRMS station at BL01, SSRF. (a) Optical layout. (b) IR beam intensity at an averaged wavenumber of 5000 cm^{-1}. An objective lens with a ×15 magnification (NA = 0.3) was used. (c) Raman spectra of D_2 measured using this facility. Reprinted with permission from A. F. Goncharov, L. Kong, and H. K. Mao, Rev. Sci. Instrum. **90**(9), 093905 (2019). Copyright 2019 AIP Publishing LLC.

necessary for pressure determination in the multi-megabar region by measuring the first-order Raman spectra of diamond anvils using red laser light. The microscope optics are designed for a variety of DAC studies, including phase transitions, changes in electronic structure, and chemical transformations. The system also has a low-temperature and ultrahigh-pressure setup, from which it is possible to collect both transmission and reflectivity mid-IR spectra using an MCT detector.

Figure 4(a) shows the optical layout of the system. Optical elements shown in blue, green, and yellow are synchrotron IR, Raman, and visible/near IR components of the system, respectively. BE, OB, PM, AP, M, RM, and SCM stand for beam expanders, objective lenses, off-axis parabolic mirrors, apertures, IR mirrors, Raman mirrors, and supercontinuum mirrors, respectively. The optical elements are positioned on the transition stages and can be positioned/removed reproducibly to change the mode of operation: OB2–OB3, M4, M7, M9, RM4, SCM2, SCM5, and AP1–AP3. Thus, one easily change the operating mode between reflectivity and transmission, as well as between various spectroscopic techniques, including Raman, visible/near-IR, and mid-IR. Two types of reflective objective lens with magnifications of ×10 and ×15, numerical apertures (NAs) of 0.23 and 0.3, and working distances of 30.6 and 24 mm are chosen for IR experiments, matching the widely used symmetric DAC of diameter 48 mm and length 36 mm, as well as the shorter symmetric B/C and BX-90 cells. By collecting IR spectral intensities approximated via the center burst amplitude when a razor blade is moved across the beam and then differentiating the resulting curves, the IR beam spot size has been estimated to be ~10 μm from the full width at half maximum, as shown in Fig. 4(b), encouraging us to plan future IR investigations at very high pressures.

For low-temperature experiments, the objective lenses, including a custom one (×8, NA = 0.25, working distance 50 mm) with a larger entrance pupil and a commercial one (×10) from Edmund Optics are used in a cryostat. A common symmetric cell can then be used at temperatures down to those achieved by liquid He cooling. A representative experiment on Raman spectroscopy of D_2 has been conducted to explore the properties of hydrogen at high pressure, and also to check the performance of the facility at low temperatures. The major vibron and roton modes of phase II of D_2 are shown in Fig. 4(c), where the splitting of rotons and the presence of the vibron sidebands indicate the presence of a rotationally ordered state. The position of the Raman edge of the stressed diamond was used to determine the pressure. These results also suggest that samples with dimensions down to 5–10 μm can be studied over a broad spectral range for both transmission and reflectivity IR measurements.

For visible/near-IR experiments, a white laser from a supercontinuum source with 400–2400 nm bandwidth is guided to the IR microscope by a flipping mirror. For visible/near-IR spectra, the data are recorded with array CCD and InGaAs detectors, which are commercially available from Princeton Instruments. The visible/near-IR studies are of particular interest for some emerging functional materials such as photovoltaic perovskites and photoluminescent quantum dots.

III. HIGH-PRESSURE SIRMS MEASUREMENTS WITH DACS

A. Diamond anvils

Depending on the amount of nitrogen impurity contained in their carbon lattice, diamonds exhibit distinct transparency behavior when exposed to UV and IR wavelengths. Diamonds containing relatively large amounts of nitrogen (~0.1%) and nitrogen-free diamonds are classified as type I and type II, respectively. Type I diamonds can be subclassified as types Ia and Ib, depending on how the nitrogen atoms are arranged in the lattice (with type Ia being further subclassified into types Ia and IIa). There is also a subclassification of type II diamonds as types IIa and IIb, depending on whether there is boron impurity contained in the diamond lattice. These various types are summarized in Table III. For high-pressure studies, mainly two types of diamonds, types Ia and IIa, are selected as anvils.[54] To enable the use of a wide range of electromagnetic radiation to characterize the physical properties of samples *in situ* at high pressures, a high transparency is required. FT-IR spectroscopy is the most widely used technique to identify diamond type, and detectable IR absorption bands from impurities can lead to difficulties in analyzing samples loaded in a DAC. Specifically, the phonon region from 400 to 1332 cm^{-1} includes the major absorption bands related to nitrogen content, which are inevitably exhibited by type Ia anvils, as shown in Fig. 5. Therefore, taking account of the band tails, if we want to study bands lower than 1500 cm^{-1}, type IIa diamond anvils are greatly preferred. For ultrahigh-pressures experiment, we also need to consider the strain state of anvils under high load, and it is sometimes necessary to use anvils with a beveled angle.

Approximately 98% of all natural diamonds contain nitrogen in various aggregate forms or as free single atoms. Such a shortage of type

TABLE III. Diamond types.

Diamond type	Impurities
Type IaA	Nitrogen atom pair
Type IaB	Group of four nitrogen atoms with lattice vacancy
Type Ib	Single nitrogen atom
Type IIa	No nitrogen or boron atom
Type IIb	Boron atom

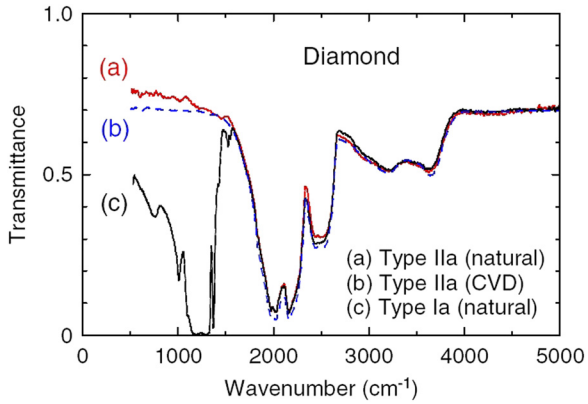

FIG. 5. IR transmittance spectra of various types of diamond anvils. Reprinted with permission from Okamura *et al.*, Jpn. J. Appl. Phys., Part 1 **56**(5S3), 05FA11 (2017). Copyright 2017 IOP Publishing.

II diamonds motivates the use of both natural and man-made diamond anvils produced by chemical vapor deposition (CVD) single-crystal growth. It has been demonstrated that CVD-grown type II diamonds exhibit almost the same hardness as natural ones, as well as having negligible nitrogen-induced absorption (Fig. 5), an essential requirement for DAC-based IR studies.[2] In addition, high-pressure, high-temperature (HPHT) treatment of diamonds can lead to a color enhancement effect that makes it possible to turn a brown diamond into a colorless one, which is of interest for visible/near-IR DAC experiments.

B. Pressure-transmitting medium

The pressure-transmitting medium (PTM) is of particular importance for accurate determination of pressure, as well as for affecting the high-pressure behavior of samples. How a suitable PTM is selected for an IR experiment depends strongly on the pressure range under study, sample properties, and measurement mode. For studies at pressures less than 10 GPa, glycerol, silicone or mineral oil, and methanol–ethanol mixtures have been employed as liquid PTMs. Their properties at high pressures have been discussed elsewhere.[55,56] These liquids usually support a high degree of hydrostaticity owing to the absence of shear stress. Besides, such liquid PTMs are cheap and readily accessible, and are easily loaded into a DAC by hand. For higher pressures, PTMs with an ambient gaseous state, such as Ne, He, and Ar, should be considered, since they enable a much higher hydrostaticity than traditional liquid PTMs. A successful gas loading process usually leads to a mild pressure of the order of 0.1–0.5 GPa, which is not appropriate for some highly compressible samples such as hybrid perovskites, since the crucial low-pressure range could then be easily jumped across. For such samples, the use of methanol/ethanol as PTM is also excluded, since organic–inorganic hybrid samples are easily decomposed, and a nonpolar solvent such as mineral oil should be employed.

Attention should be paid when conducting high-pressure IR reflectance experiments, which require sufficiently close contact between sample and diamond to avoid a thin gap that can lead to interference between the light reflected from the sample and that reflected from the diamond surface. Thus, solid PTMs such as NaCl and KBr are used, although they provide inferior hydrostaticity to liquid PTMs.

C. Gasket and sample preparation

Usually, stainless steel T301 with an initial thickness of ~250 μm is the first choice as gasket material for high-pressure studies at less than 50 GPa. For much higher pressures, less-deformable metals such as tungsten (W) and rhenium (Re) should be considered, and W gaskets are also used for investigating samples with magnetic properties. Before drilling the gasket hole for containing samples, a pre-indentation process is conducted by applying pressure directly on the plate, resulting in a gasket with a much decreased thickness and with a particular anvil shape. The size of the gasket hole (sample chamber) is designed to be one-third the size of the anvils, which helps it to maintain its shape under high pressure. It should be noted that since the sample thickness has an important effect on the profile of the IR absorption spectrum, the sample loading process should be conducted many times to determine a suitable thickness. For IR reflectance experiments, a sample with a highly flat surface should be loaded and attached tightly to the surface of the anvil on one side.

D. Transmission and reflectance measurements

There are two operating modes for a SIRMS experiment (as for an in-laboratory IR experiment), namely, transmission and reflectance measurements. Transmission is the ability of a material to allow electromagnetic radiation such as IR radiation to pass through it. The transmission spectrum $T(\omega)$ of a sample can be described as

$$T(\omega) = \frac{I(\omega)}{I_0(\omega)}, \tag{4}$$

where $I(\omega)$ and $I_0(\omega)$ are the frequency-dependent intensity spectra after the incident IR radiation has passed through the sample and background, respectively. The absorbance spectrum $A(\omega)$ can be derived from the transmission spectrum as follows:

$$A(\omega) = \log\frac{1}{T(\omega)}. \tag{5}$$

For IR experiments, measurements need to be performed on both background and sample. The signals from both measurements contain information from the PTM and the two diamond anvils. Therefore, when the sample is loaded in the gasket hole (sample chamber), the transparent space not occupied by sample should be used for collecting background data. Alternatively, two holes should be drilled in the same gasket, with one containing only PTM for background testing and the other containing both PTM and the sample to be studied. It should be noted that the transmission signal is strongly dependent on the sample thickness. A very thin sample usually has an ultrahigh transmissivity, and thus it is generally difficult to derive its $T(\omega)$ function in a DAC if the differences between the profiles of $I(\omega)$ and $I_0(\omega)$ are not readily detectable. On the other hand, an excessively thick sample will have nearly zero transmissivity, which also makes it difficult to obtain reliable results and leads to oversaturated $A(\omega)$ data. Thus, some initial tests to optimize the sample thickness need to be carried out before high-pressure IR experiments. As the applied pressure increases, the intensities of $A(\omega)$ and $T(\omega)$ could change greatly, since the sample in the DAC will become much thinner.

As radiation is incident from a medium onto a surface, it may be reflected, transmitted, or absorbed, and the respective magnitudes of reflection and transmission are determined by the angle of incidence and the refractive indices of the two media. The refractive index of a material is linked to its absorption of radiation. Specifically, in cases where only reflectance spectra can be measured, the Kramers–Kronig transformation is useful to obtain absorbance and refractive index information from reflectance data. The reflectance spectrum from an optically dense material will be a complex spectrum with two components: the absorbance spectrum and the refractive index spectrum. The Kramers–Kronig analysis is able to extract these two components from the complex reflectance spectrum. This analysis assumes reflectance angles near zero. The output of the transformation depends strongly on the quality of the measurements, and artifacts in the low-wavelength region need to be eliminated properly or the transformation will yield inadequate results. From the IR reflectance spectrum and further Kramers–Kronig analysis and profile fitting, it is possible to obtain optical conductivity functions,

which is a crucial task in studies of various high-pressure phenomena, ranging from metallization to superconductivity subgaps. To obtain a reliable IR reflectance spectrum R of the sample–diamond surface in a DAC, some corrections are required. First, to minimize the errors associated with the diminishing beam intensity caused by ring current decay, it is necessary to measure the reflectivity R_d of the air–diamond interface before focusing the beam on the sample being studied. To normalize the reflectance spectrum, we generally use an Au film placed in the sample chamber. The following relationships then hold:

$$I_d = I_0 R_d, \tag{6}$$

$$I_e = I_0 R_d (1 - R_d)^2 (1 - A_d)^2, \tag{7}$$

$$I_s = I_0 R (1 - R_d)^2 (1 - A_d)^2, \tag{8}$$

where I_d, I_0, I_e, and I_s are the powers reflected off of the diamond–air interface, the air–Au interface, the diamond–air interface (through the diamond), and the diamond–sample interface, respectively, and A_d is the absorptivity of diamond. From Eqs. (6)–(8), the reflectance spectrum $R(\omega)$ can be expressed as

$$R(\omega) = \frac{I_s}{I_e}\frac{I_d}{I_0} \tag{9}$$

and can be indirectly obtained from *in situ* experiment at every pressure point.[57]

IV. RESEARCH EXAMPLES

A. Hydrogen

As the simplest element, hydrogen has served as a fundamental testbed for many theories in physics. To test current theoretical models of the behavior of hydrogen at high pressures and understand recent experimental results, detailed knowledge is required of the pressure-induced transitions from low-density molecular hydrogen with quantum-solid behavior to the expected metallic molecular solid and eventually to an atomic metal.[58–63] The interaction between H_2 molecules is responsible for the transitions of the system, which involve not only the lattice structure but also the arrangement and motion of molecules, and this interaction dominates the properties of hydrogen solids via its effect on the internal properties of the molecules. Several pioneering experimental studies involving Raman and IR measurements have been devoted to investigate the electronic properties of hydrogen solids,[64–70] the result of which have provided qualitative or semiquantitative information about the intermolecular interaction. To study pure compressional effects, the Raman vibron frequency of H_2 molecules embedded in an Ne matrix has been measured at pressures up to 45 GPa.[64] The monotonic increase in the Raman shift with pressure in these isolated H_2 molecules is in strong contrast to that measured in pure solid hydrogen, which exhibits a maximum at around 30 GPa.[67] Such a large difference and the turnover of the vibron frequency in pure hydrogen can be understood in terms of the balance between decreasing bond length and increasing dielectric constant with pressure,[71] where both the surrounding medium and the pure pressure effect play important roles and the mean-field expression for the collective properties is taken into account. In the megabar range, the turnover in the IR vibron frequency has been revealed by a synchrotron IRS technique, where the frequency difference between out-of-phase IR and in-phase Raman-active H–H stretching $Q_1(1)$ modes has been shown to increase from 3 cm^{-1} at zero pressure to 510 cm^{-1} at 180 GPa, giving a measure of bandwidth with pressure, and also indicating increased intermolecular interaction in hydrogen solids.[65]

With the advent of SIRMS, it has become possible to perform optical studies on solid hydrogen under ultrahigh pressures. Not only has the pressure range been greatly extended, but in addition the combination of IR techniques with other characterization tools has been introduced. The strength of intermolecular coupling can be demonstrated by the value of the Raman–IR splitting value, because Raman and IR vibron modes exhibit distinct features for molecules in a same unit cell: out-of-phase for IR and in-phase for Raman-active modes.[61] For accurate characterization of the splitting, a large uncertainty in pressure determination should be avoided, and thus a combined concomitant IR–Raman system is preferred rather than separate IR and Raman facilities. By employing the system at SSRF, which combines SIRMS with Raman spectroscopy (for details, see Sec. II B), together with toroidal diamond anvils with 30 μm sized culets, it has been possible to obtain relatively precise intermolecular couplings of hydrogen up to 280 GPa on the same sample.[72] As shown in Fig. 6, above 230 GPa, the coupling is sharply increased for molecules belong to graphene-like layers (G-layers) while for Br_2-like layer (B-layer) molecules, the coupling is clearly weaker, suggesting that G-layer molecules in hydrogen phase IV are highly fluxional.

This behavior is consistent with previous IR studies performed at SOLEIL, which indicated the existence of a partially ordered structure of hydrogen where the molecules were ordered in one layer and partially disordered in alternate layers.[73]

The above vibrational spectroscopy results provide crucial information to determine the molecular order in the alternating layers, which cannot be resolved by x-ray diffraction (XRD), and they play an

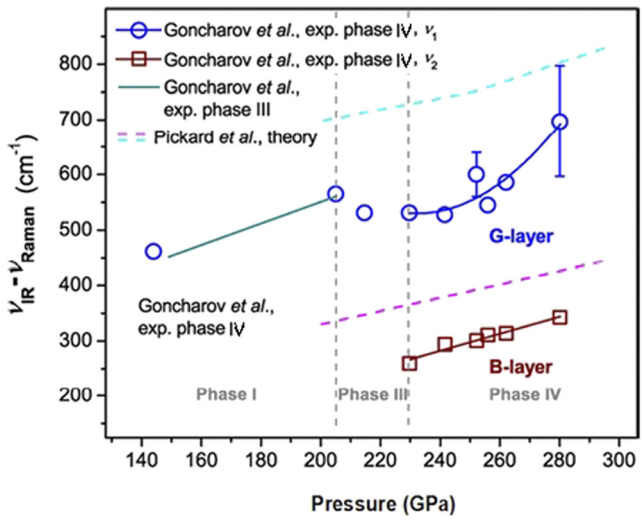

FIG. 6. Pressure dependence of intermolecular coupling represented by the difference between the IR and Raman vibron frequencies up to 280 GPa. Reprinted with permission from Goncharov *et al.*, Proc. Natl. Acad. Sci. U. S. A. **116**(51), 25512–25515 (2019). Copyright 2019 National Academy of Sciences.

important role in theoretical investigations of lattice dynamics. In addition, IR vibrational spectroscopy is complementary to XRD in determining phase transition behavior arising from sensitivity to local symmetry. A vibron Raman frequency discontinuity of −15 cm^{-1} and the appearance of a strong IR vibron at 215 GPa have been demonstrated to be features of a I–III transition, while at 237 GPa, a vibron Raman frequency discontinuity of −55 cm^{-1} (with a change in slope of the frequency shift) and the appearance of a second IR mode at a frequency above 4400 cm^{-1} are believed to be associated with a III–V phase transition of hydrogen.[73]

Theorists have long predicted that hydrogen will be a metal at very high pressures, and it has also been predicted that such a dense metallic solid could possess many unusual properties, such as combined superconductivity and superfluidity. Therefore, over the years, there have been many experimental searches for this material, and the discovery of metallic hydrogen has become one of the principal goals of high-pressure research. It should be pointed out that the most rigorous way to identify a metal is to measure the temperature dependence of its conductivity. However, such measurements are extremely difficult in DACs, since they rely on putting tiny electrodes on the tip of a diamond and in contact with a minute amount of high-pressure solid hydrogen, and very few such measurements have been attempted.[74] As an alternative approach, investigators have relied on characterizing the IR reflectivity based on the Drude free-electron model and/or observing a bandgap closure *in situ*. In particular, a direct determination of optical conductivity can be done on the basis of IR spectroscopy at long wavelengths, thereby providing an essential indication of metallization if this does indeed occur. These measurements require a broad range of frequency below the plasma frequency. In the 1990s, replacement of Globars by sources based on thin-walled graphite tubes extended the low-frequency limit from 3000 to 1000 cm^{-1}, and no Drude behavior was observed in solid hydrogen at 191 GPa and low temperatures.[75] Synchrotron radiation was then introduced to provide a high-flux, broadband IR source approaching the far-IR region, making it possible to identify whether a more compressed sample can reflect IR wavelengths at lower frequencies, as well as enabling measurement of the transmission at the longest wavelengths allowed by the diffraction limit of the small samples (usually <10 μm aperture) at multi-megabar pressures. Figure 7 shows synchrotron IR absorption spectra of hydrogen up to 360 GPa from 12 to 300 K, from which it can be seen that the sample is still transparent at energies down to 0.1 eV, and thus no evidence of a metallic state is present.[76]

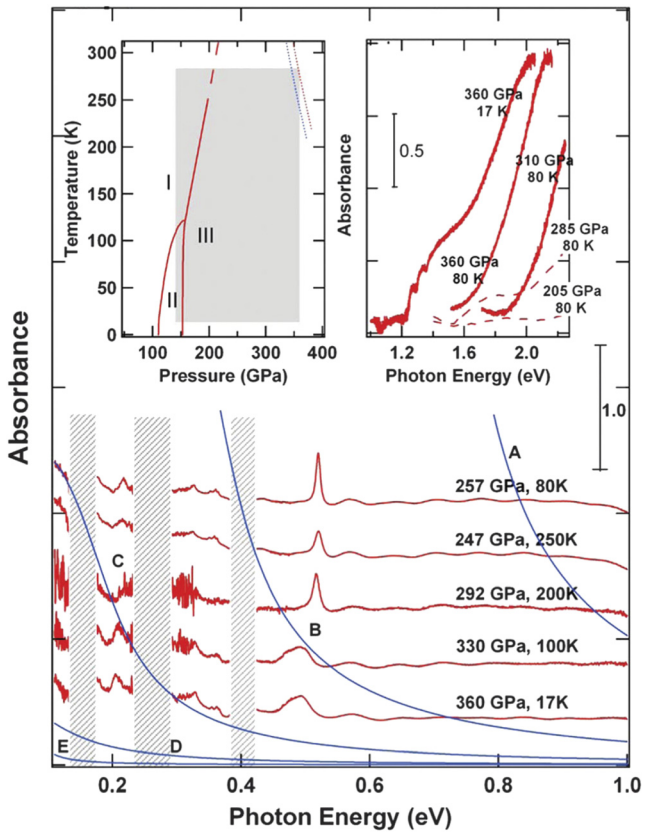

FIG. 7. Selected absorption spectra of hydrogen at high pressure and low temperature. The shaded areas are regions of absorption from diamond anvils at low energy, and the blue curves are representative optical conductivities derived from the simple Drude model. The left inset shows the pressure–temperature phase diagram of hydrogen, where the highlighted area is the region of study. The right inset shows the visible absorption spectra at selected pressures and temperatures. Reprinted with permission from C.-S. Zha, Z. Liu, and R. J. Hemley, Phys. Rev. Lett. **108**(14), 146402 (2012). Copyright 2012 American Physical Society.

It is clearly necessary to further extend the accessible pressure range to study highly dense hydrogen. To this end, Loubeyre *et al.*[77] used a toroidal DAC with specially formulated diamond tips that could withstand pressures up to 427 GPa, They then employed a SIRMS station at SOLEIL that enabled them to simultaneously measure multiple properties of hydrogen in the DAC.[77] Their results have been cited as direct evidence of "the probable transition to metal hydrogen," representing a great a technical breakthrough, although a small bandgap cannot be totally ruled out at the highest pressure achieved in their work. Figures 8(a) and 8(b) show the discontinuous pressure evolution in the absorption and the pressure dependence of the bandgap, respectively. It is noteworthy that the maximum measurable absorbance value is just 2 [Fig. 8(a)], from which the possible existence of a small bandgap can be inferred, with an uncertainty of less than 0.14 eV as estimated from the thickness of the hydrogen sample. In addition, as Loubeyre *et al.* stated, they could not rule out a direct bandgap less than 0.1 eV because of the lack of data covering the spectral range below 800 cm^{-1}. In the future, more evidence for metallic hydrogen, such as detection of the Drude mode by IR reflectivity, could be examined, and it should also be interesting to look for other unusual properties of hydrogen in this newly accessible temperature–pressure range.

B. Nitrogen

Similar to atomic metallic hydrogen, single-bonded nitrogen has been postulated to be one of the ultimate energetic materials owing to its high energy density. Ultrahigh pressures of the order of several gigapascals are required to obtain such materials, and, given the high compressibility of N_2, and starting as a gas at ambient pressure, it is extremely difficult to resolve its structure at ultrahigh pressures using small samples. Therefore, again similar to the case of

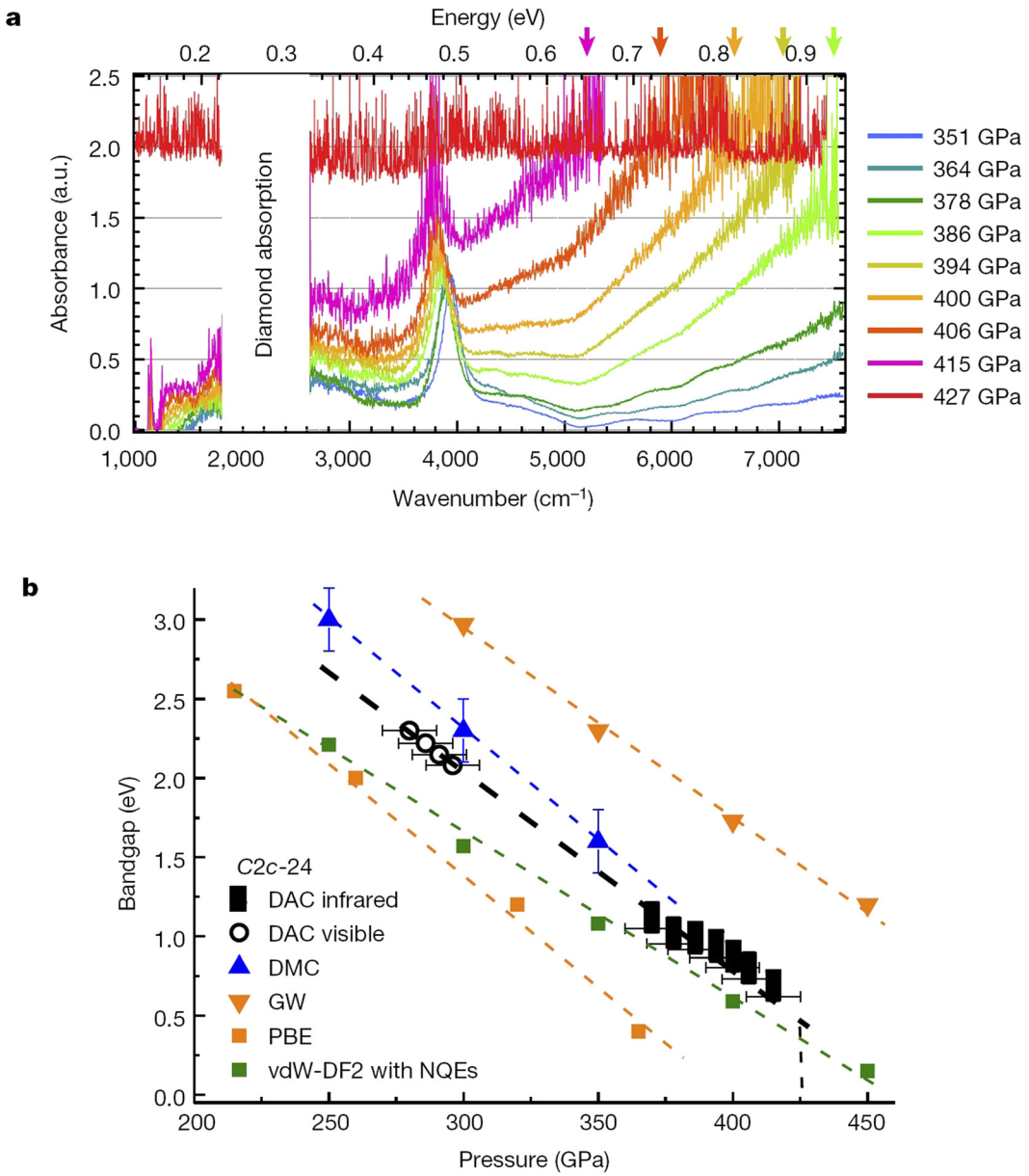

FIG. 8. (a) Selected absorption spectra of hydrogen at high pressures up to 427 GPa. The arrows denote the magnitude of the bandgap. (b) Pressure dependence of bandgap from experiments and calculations. Reprinted with permission from P. Loubeyre, F. Occelli, and P. Dumas, Nature **577**(7792), 631–635 (2020). Copyright 2020 Springer Nature Limited.

hydrogen, studies on nitrogen have also taken advantage of DACs and recent developments in synchrotron-based techniques.

The crystalline and electronic structures of highly dense nitrogen have been comprehensively investigated, and various phases have been discovered, with IR spectroscopy playing a crucial role in this work.[78–80] By employing IR and Raman characterizations, Bini *et al.*[79] studied the phase transition behavior of nitrogen between 25 K and room temperature and up to 41 GPa, and were able to plot the phase boundary between δ and ε phases in the range 30–230 K. From the pressure dependence of the frequencies of the Raman and IR vibrational modes, it was found that vibrational coupling among neighboring molecules is negligible in δ phase but appears in the ε phase owing to an orientation freezing effect. At pressures less than 120 GPa, it has been found that nitrogen exists as triple-bonded molecules with weak van der Waals interactions, and at least seven triple-bonded phases ($\alpha, \beta, \gamma, \delta, \varepsilon, \lambda$, and ζ) have been identified, thus revealing a complicated P–T phase diagram.

The lower-pressure stable phases have much lower energy capacities than their single-bonded counterpart, and the latter has only been observed at higher pressures. Above 150 GPa, Goncharov *et al.*[80] found that nitrogen becomes totally opaque and electrically conductive. Figure 9 shows IR absorption spectra of nitrogen in the 80–170 GPa range at room temperature, from which it can be seen that the N_2 molecular vibrational IR peak disappears and a new broad peak appears. This change in vibrational excitations, together with the appearance of a low-energy bandgap, indicates that a transition occurs from the molecular phase to a nonmolecular phase, which is also supported by Raman results obtained from the same sample. Of particular interest is the weak IR peak at ~900 cm^{-1} at 170 GPa (Fig. 9). From a comparison of experimental and theoretical results, the appearance of a lattice mode as a result of the transition suggests the presence of the long-sought-after polymeric nitrogen with the predicted cubic *gauche* structure (cg-N), which has indeed been synthesized above 2000 K and 110 GPa using a laser heating method. Considering that an XRD Bragg peak has not been found and that the linewidth of the IR/Raman mode is relatively large, it is reasonable to believe that at room temperature the high-pressure phase could be a fine mixture of various structures, exhibiting long-range disorder with possible local ordering.

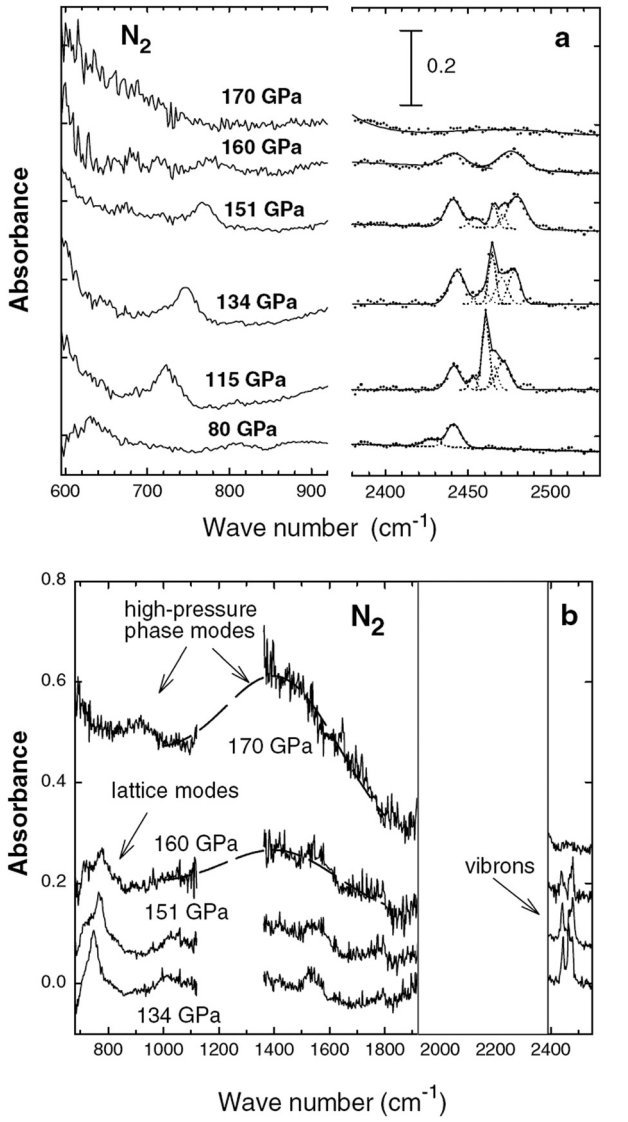

FIG. 9. (a) Selected absorption spectra of nitrogen at high pressures from 80 to 170 GPa at room temperature. (b) High-pressure lattice modes found above the phase transition pressures. Reprinted with permission from Goncharov *et al.*, Phys. Rev. Lett. **85**(6), 1262–1265 (2000). Copyright 2000 American Physical Society.

C. Sulfur hydride

Superconducting transition temperatures T_c of 203 K in H_3S and 250–260 K in LaH_{10} were reported by Drozdov *et al.*,[81,82] while Snider *et al.*[83] observed superconductivity at an even higher temperature of 287 K in a carbon-modified sulfur hydride material. So far, high pressures are inevitably required to obtain these dense-phase hydrides. However, studies of these novel compounds could provide crucial guidelines for attempts to achieve superconductivity at ambient pressure and room temperature by considering alternative chemical doping strategies. In this context, although calculations using density functional theory (DFT) suggest that the mechanism of superconductivity in hydrides is based on electron–phonon interaction originating from light-mass hydrogen and strong coupling to high-energy modes,[84–88] direct experimental evidence is urgently required for the development of future superconducting materials.

Capitani *et al.*[89] designed a synchrotron-based far-IR experiment to provide spectroscopic evidence of a conventional mechanism for the superconductivity in H_3S (Fig. 10). They employed reflectance rather than transmission measurements, since the latter require extremely thin samples of the order of tens of nanometers and so are difficult to realized in a DAC. Several technical approaches based on these measurements have been considered, including exploring the temperature dependence of the reflectivity ratio R_s/R_n between superconducting and normal metal states, as well as using either the diamond surface or the NaCl insulating layer as a reflectance reference to deal with problems arising from the small size of the sample and the presence of diamond. Figure 10(a) shows the calculated reflectivity ratios R_s/R_n for H_3S in the two superconducting states (at 50 K for the well-established superconducting state and at 150 K close to T_c) compared with the normal metal state at 200 K. Three regions can be identified: a gap region (<100 meV), a phonon absorption region (100–300 meV), and a boson region (300–600 meV). As shown in Fig. 10(b), a peak feature is found at 76 meV, which is consistent with the calculated value of the superconducting gap, 73 meV. An exploration of the bosonic structure [Fig. 10(c)] demonstrates that H_3S becomes a better reflector with increasing temperature, further supporting an electron–phonon interaction mechanism according to Eliashberg theory. Of particular interest is the strong absorption by active phonons with a minimum at 153 meV [Fig. 10(d)]. This observation can be reproduced by a two-component model containing a Drude peak and a Lorentz oscillator, in which the enhanced strength of phonons is due to a considerable contribution from electronic degrees of freedom.

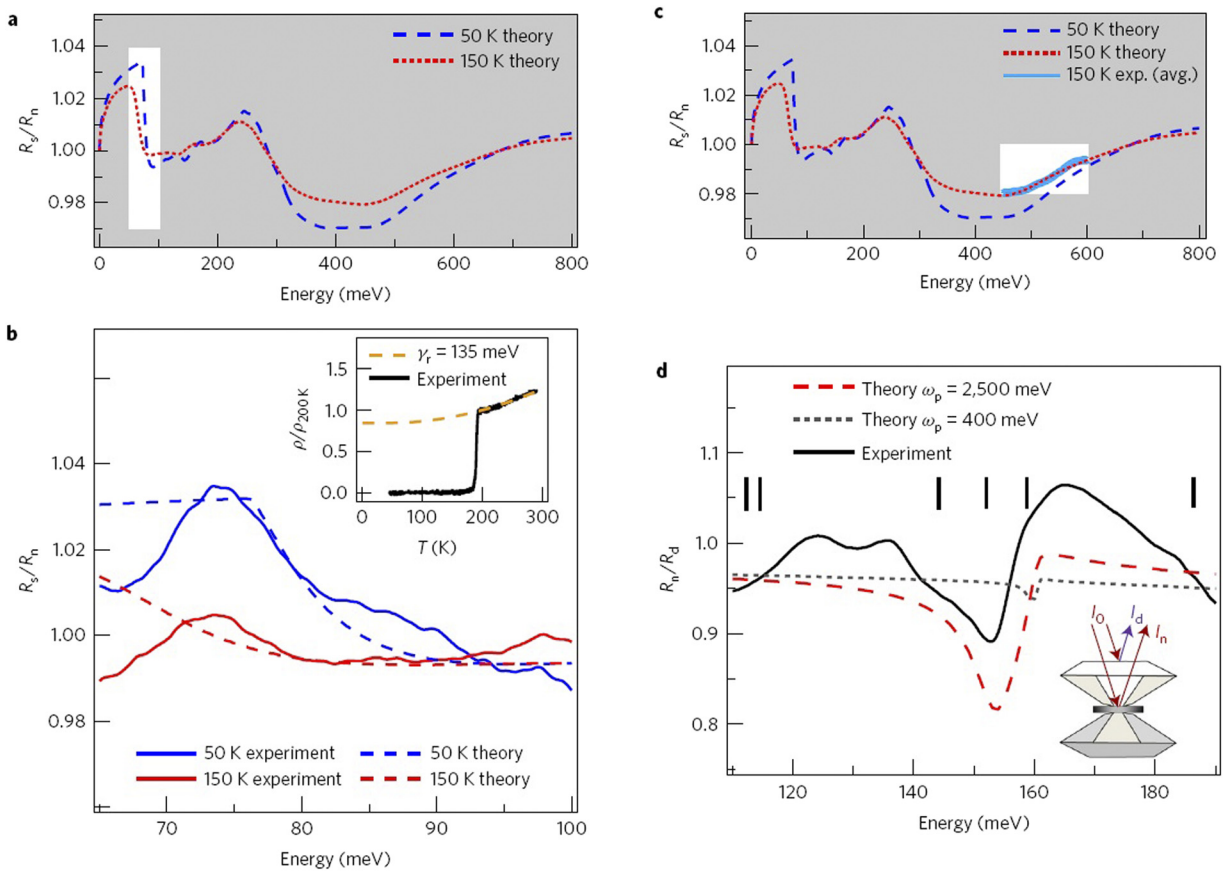

FIG. 10. (a) Calculated reflectivity ratios R_s/R_n of H_3S in the two superconducting states (at 50 and 150 K) compared with the normal metal state at 200 K. (b) Superconducting gap measurement. (c) Bosonic structure study showing an agreement between theoretical and experimental results and demonstrating an electron–phonon interaction mechanism. (d) Strong absorption due to IR-active phonons. Reprinted with permission from Capitani *et al.*, Nat. Phys. **13**(9), 859–863 (2017). Copyright 2017 Springer Nature Limited.

D. Metal–organic frameworks

Metal–organic frameworks (MOFs) are a family of chemically diverse materials consisting of metal ions or clusters coordinated to organic ligands.[90–94] Owing to their large porosities, MOFs have industrial applications for gas storage.[95–97] It has been demonstrated that the high pressures realized by the DAC technique, which are far beyond the gas absorption pressure, could promote the incorporation of large molecules in MOFs. In addition, pressure also enhances the ability of MOFs to store greenhouse gases. For these materials, SIRMS provides not only direct experimental evidence for gas storage, but also an understanding of local structure, chemical bonding, and the interactions between MOFs and absorbed molecules.

Using SIRMS, Hu *et al.*[98] loaded a ZIF-8 framework (a representative member of the important zeolitic imidazolate-based family of MOFs) together with CO_2 in a DAC and studied the gas storage behavior under high pressure. The hexagonal channels of ZIF-8 are a bit larger than the kinetic diameter of the CO_2 molecule (0.34 nm vs 0.33 nm). Together with the pressure-driven lattice expansion of the framework, it is not surprising to observe an enhanced and pressure-dependent storage of CO_2 in the framework. Figure 11 shows the IR absorption spectra of pure CO_2, pure ZIF-8, and a ZIF-8/CO_2 mixture at relative low pressures of the order of 0.8–1.0 GPa, from which distinct profiles can be identified. The CO_2 overtone/combination bands $\nu_3 + \nu_1$ and $\nu_3 + 2\nu_2$ were used to investigate the insertion of gas into the pores of the ZIF-8 framework (the inset of Fig. 11). For pure CO_2, these two bands are originally at 3708 and 3604 cm^{-1}, respectively, while for the ZIF-8/CO_2 mixture each band splits into two peaks, with the low-frequency component resembling the overtones of pure CO_2 that is still outside the framework and the sharper and intense high-frequency component coming from the considerable portion of CO_2 that has already been inserted into the pores under pressure. In addition, from the IR absorption profile of the ZIF-8/CO_2 mixture, a new C=C stretching mode of the imidazole ring at 1620 cm^{-1} is found, indicating that the interaction between CO_2 and the ZIF-8 framework occurs at some specific sites of the imidazole ring.

Owing to the existence of organic groups, the lattices of MOFs are generally very soft. These soft materials have the property that even very mild pressure will lead to detrimental lattice distortion and weakening and thus to performance degradation. From *in situ* observations of gas storage behavior, it can be seen the lattice disorder

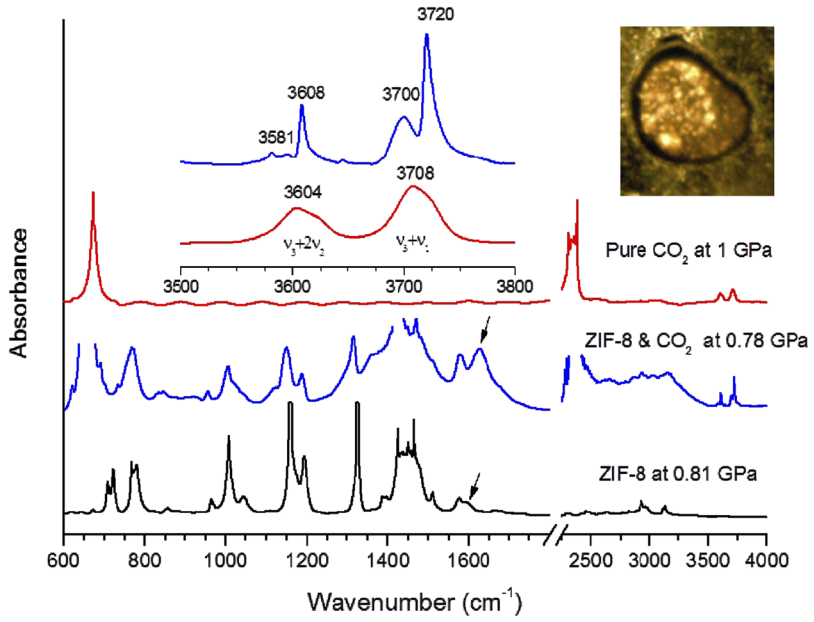

FIG. 11. IR absorption spectra of pure CO_2, pure ZIF-8, and ZIF-8 loaded with CO_2 at mild pressures of the order of 0.78–1.0 GPa. The left inset shows the zoomed spectral region of 3500–3800 cm^{-1}. The right inset shows a photograph of ZIF-8 loaded with CO_2. Reprinted with permission from Hu *et al.*, J. Am. Chem. Soc. **135**(25), 9287–9290 (2013). Copyright 2013 American Chemical Society.

and peculiar lattice expansion of MOFs under pressure is strongly dependent on the PTM in a DAC. Celeste *et al.*[99] studied the behavior of MIL-101 (a member of another class of MOFs) under high pressure using SIRMS. As a solid PTM (NaCl) was employed, they found that an irreversible crystal-to-amorphous transition started at very low pressure, ~0.1 GPa. On the other hand, they found that the stability of the framework was significantly enhanced by using a fluid PTM such as Nujol or high-viscosity polydimethylsiloxane silicone oil. The mechanism was further revealed as fluid PTM penetration inside the pores, postponing the pressure-driven amorphization to 7 GPa, and the accompanied lattice expansion was found to be associated with the concomitant nucleation of a denser amorphous phase. These results shed some light by suggesting the use of a high-pressure technique to obtain better and more stable MOFs as well as to enlarge the range of potential applications.

E. Metal halide perovskites

Understanding how the modulation of lattice structure alters electron wave functions in materials is important when establishing a mechanistic foundation for various applications of material properties such as superconductivity, thermoelectricity, photovoltaics, and photoluminescence. For example, the emerging organic–inorganic hybrid lead triiodide perovskite materials have the potential to provide the basis for a low-cost and high-efficiency photovoltaic technology.[100–103] As a powerful and clean tool, hydrostatic pressure represents a promising approach to precisely modulate the crystal lattice of materials and pinpoint their electronic behaviors. There has been significant progress in research into high-pressure halide perovskites in the last few years, including reliable determination of structure–property relationships, the discovery of pressure-driven novel properties, and the realization of novel functionalities, as well as the advent of pressure/strain engineering for quenchable materials as the applied pressure is totally removed.[32,104–107]

With the addition of SIRMS, the development of DAC-based characterizations has enabled clarification of the pressure-driven phase transition and pressure-driven metallization behaviors of various metal halide perovskites. Using controllable hydrostatic pressure to modulate bond lengths and bond angles, it has turned out to be possible to achieve synergistic enhancement of two key photovoltaic properties, namely, bandgap narrowing and carrier lifetime prolongation, in methylammonium lead iodide perovskite ($CH_3NH_3PbI_3$) under mild pressures ~0.3 GPa.[108] Such enhancement is crucial for further progress in energy conversion efficiency, and the structure–property relationship involves a pressure-driven structural evolution mechanism that can be revealed by *in situ* SIRMS measurements. As pressure rises, both blue- and redshifts are observed in characteristic modes (Fig. 12). For the $-CH_3$ stretching mode, no significant changes in frequency were observed in the low-pressure phase (between 1 atm and 0.4 GPa), while a notable blueshift was observed as the pressure exceeded 0.4 GPa, owing to a phase transition. In these high-pressure phases, the volume of the lattice underwent considerable shrinkage, leading to strong repulsion between the inorganic PbI_3^- framework and the electron waves on the H atoms in the methyl group. Hence, the frequency of C–H stretching increased. The same rationale can also be applied to explain the blueshift of the C–N stretching above 0.4 GPa. Both the N–H stretching and bending modes in the NH_3^+ experienced redshifts as the pressure increased. This opposite trend of the N–H modes compared with the C–H and C–N modes can be attributed to the cationic charge on $CH_3NH_3^+$, which is well known to be localized to the three

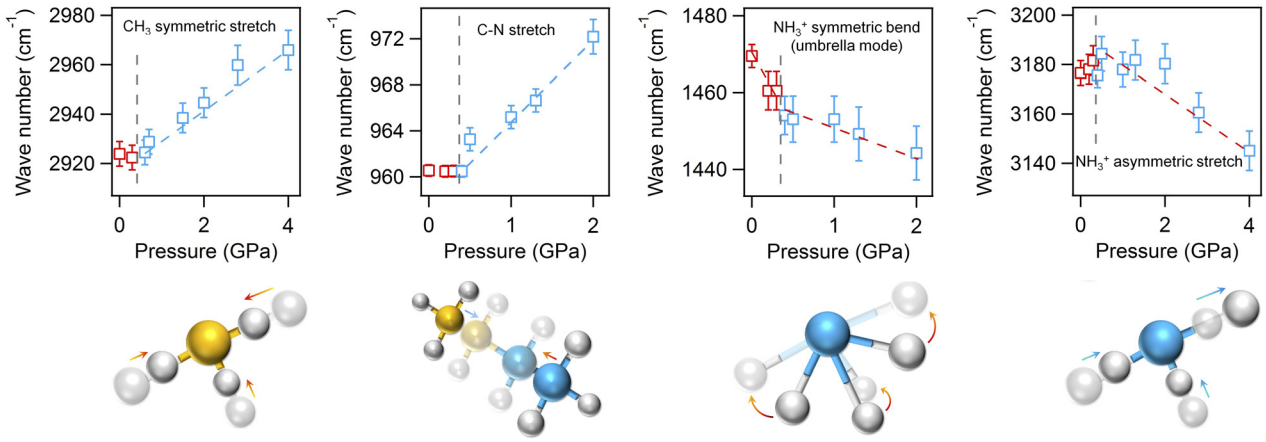

FIG. 12. Pressure dependence of frequencies for four mid-IR modes. Pressure-driven IR peak shifts are distinguished between low-pressure and high-pressure phase ranges. Red and blue open squares represent the peak positions of the IR modes measured in the low-pressure range corresponding to the *I*4/*mcm* phase and in the high-pressure range corresponding to the *Imm*2 phase, respectively. Gray dashed lines indicate the approximate phase boundaries. Red dashed and blue dashed lines are guides to the eyes for redshifts and blueshifts. Reprinted with permission from Kong *et al.*, Proc. Natl. Acad. Sci. U. S. A. **113**(32), 8910–8915 (2016). Copyright 2016 National Academy of Sciences.

hydrogen atoms connecting to the nitrogen. Therefore, the pressure-induced lattice shrinkage further enhanced the electrostatic attraction between the cationic charge on the nearly naked protons in NH_3^+ and their neighboring anionic charge on the PbI_3^- framework, slowing down the modes in NH_3^+. Note that such information about local structural evolution cannot be obtained from long-range characterization tools such as XRD and neutron diffraction, emphasizing the importance of IR spectroscopy in painting the full picture of structure–property relationships in high-pressure materials science.

The availability of high pressures has opened the way to revealing new properties of known metal halide perovskites, where unusual phenomena that do not exist under ambient conditions have been found. By measuring absorption spectra across visible and IR wavelengths, Jaffe *et al.*[109] monitored the bandgap evolution of $CH_3NH_3PbI_3$ under applied pressures up to 64 GPa, from which a semiconductor–metal transition was demonstrated by bandgap closure in this highly amorphous material [Fig. 13(a)]. This metallization was further supported by the observation of Drude modes at low frequency from IR reflection measurements [Fig. 13(b)] and was later confirmed by the measured temperature dependence of the conductivity at various pressures. The metallization behavior in halide perovskites could be affected by an isotope effect.[110] Comprehensive high-pressure experiments have showed that the photoluminescence intensity and mechanical stability of $CH_3NH_3PbI_3$ are dramatically improved when hydrogen is replaced by the heavier deuterium in the organic cation. $CD_3ND_3PbI_3$ will endure twice as much external pressure as $CH_3NH_3PbI_3$.[110] The threefold increase in photoluminescence intensity resulting from this improved lattice stability has previously been unachievable without isotope doping. The improvement originates from the suppression of lattice disorder by the less dynamic $CD_3ND_3^+$ cations, which maintain long-range crystalline order through steric and Coulombic interactions. Note that the highly disordered state is a requisite step for extreme overlap of electronic wave functions, which finally leads to metallization. Thus, delayed bandgap closure should be expected in $CD_3ND_3PbI_3$, and this has indeed been shown by SIRMS experiments [Fig. 13(c)]. These observations suggest that isotopic effects can be used to engineer electronic structure and transport properties through changing lattice stability, which is somewhat contrary to current understanding. In addition, IR tools can be employed not only to study possible changes in properties due to order–disorder transition, but also to identify the order–disorder transition itself by measuring the broadening of vibrational bands.

F. Hydrous minerals

Water controls igneous activity, tectonics, the rheology of rocks, and various temperature-dependent geochemical reactions on the Earth.[111–113] Specifically, H_2O in hydrous minerals is a main carrier playing a crucial role in hydrogen release, superoxide production, oxygen-rich pile formation, and net oxygen gain in the Earth's mantle. The behavior of hydrous minerals is strongly associated with the properties of hydrogen bonds, which affect compressibility, stability, and thermodynamics.[114–116] When integrated with DAC-based technique, IRMIS is a powerful and particularly suitable tool for investigating hydrous minerals under high-pressure conditions for the following reasons: (i) changes in the strength of hydrogen bonds are usually estimated based on frequency shifts in OH-stretching modes, which can be directly derived from IR results; (ii) a quantitative characterization of the water content of minerals can be obtained from IRS owing to its high sensitivity; (iii) at high pressures, hydrous minerals are highly disordered. In this context, XRD and neutron diffraction cannot provide accurate crystalline structures and only give some average information based on broad peaks. In addition, x-rays are scattered more effectively by heavy atoms with many electrons than by light atoms such as oxygen and hydrogen, the relative positions of which are therefore very difficult to obtain. In the case of neutron diffraction, although this has high sensitivity in the detection of light elements, the small sample size in high-pressure experiments clearly excludes many neutron investigations.

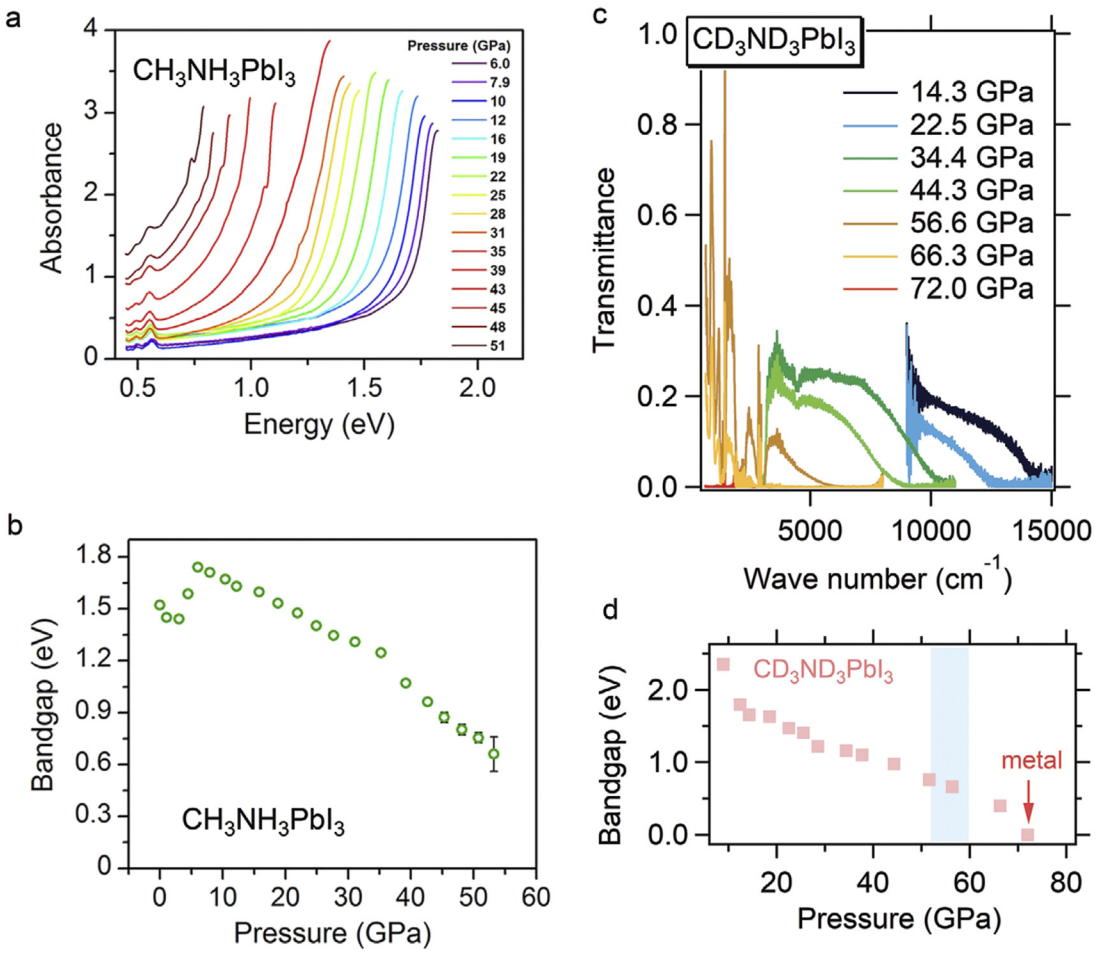

FIG. 13. Pressure-induced metallization in methylammonium lead iodide perovskite: (a) and (b) $CH_3NH_3PbI_3$; (c) and (d) $CD_3ND_3PbI_3$. In (d), the blue-shaded region indicates the pressures where metallization of $CH_3NH_3PbI_3$ takes place. (a) and (b) Reprinted with permission from Jaffe *et al.*, J. Am. Chem. Soc. **139**(12), 4330–4333 (2017). Copyright 2017 American Chemical Society. (c) and (d) Reprinted with permission from Kong *et al.*, Adv. Funct. Mater. **31**(9), 2009131 (2021). Copyright 2021 John Wiley & Sons, Inc.

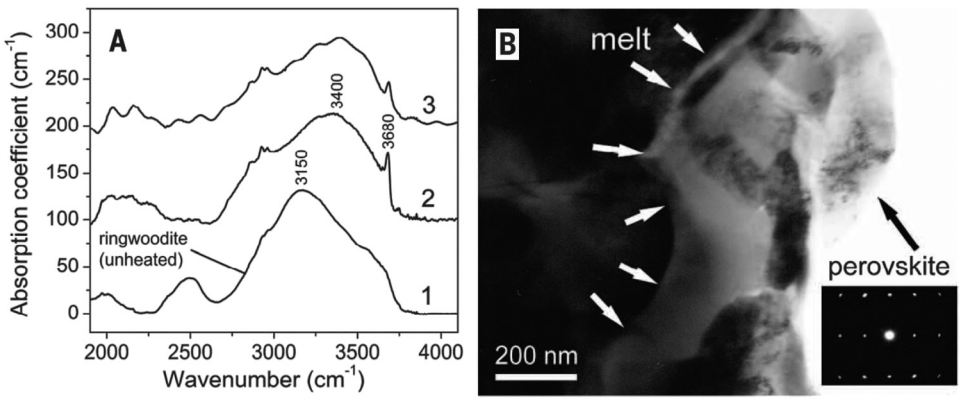

FIG. 14. (a) Synchrotron IR absorption and (b) TEM characterizations of hydrous ringwoodite sample recovered from 30 GPa. In (a), spectrum 1 refers to the detected location in the unheated part of the crystal. The other locations 2 and 3 were laser-heated at 1600 ˚C. Reprinted with permission from Schmandt *et al.*, Science **344**(6189), 1265–1268 (2014). Copyright 2014 American Association for the Advancement of Science.

Negative and positive frequency shifts in OH-stretching modes indicate strengthening and weakening of hydrogen bonds, respectively. Considering the strong interlinkage between hydrogen bonding and the crystalline framework in hydrous minerals, the variations in OH frequency with pressure can be employed to study phase stability. Figure 14 shows SIRMS and transmission electron microscopy (TEM) characterizations of a hydrous ringwoodite sample recovered from 30 GPa, which was heated at 1600 °C. After laser heating, the maximum in the OH-stretching absorbance shifted from 3150 to 3400 cm^{-1} and a sharp peak was observed at 3680 cm^{-1}.[117] The broad OH band indicates a disorder feature (a melt), and the new peak clearly demonstrates a ringwoodite-to-perovskite phase transition, this is further supported by the TEM result and is evidence that dehydration melting can lead to an H_2O trap at the top of the lower mantle.

Some important thermodynamic data, such as heat capacity and entropy, can be calculated from absorption IR and Raman spectra. An accurate calculation needs good band assignment, an appropriate model, and high-quality absorption data. In this context, the use of IR radiation from a synchrotron light source is crucial, giving a broad detection range down to the far-IR at high pressures and enabling all (or at least more) fundamental IR modes to be observed. Further details of this research and the models employed can be found in Ref. 118.

V. CONCLUDING REMARKS

IR microspectroscopy, originally a tool for structural investigations and imaging, is nowadays successfully integrated with high-flux synchrotron light sources and has been used in many areas in physics, chemistry, materials science, and geosciences. With the addition of DAC-based techniques, tremendous progress has been made in recent decades in employing SIRMS to characterize condensed matter at high pressures. From IR spectra, we have witnessed that pressure dramatically changes a diverse range of properties, such as crystal phase, lattice dynamics, bandgap, and electronic structure, providing evidence of interesting phenomena such as metallization and gas storage. Underlying mechanisms, such as electron–phonon interaction in high-temperature superconductors, have been revealed and are of fundamental importance for future applications.

Research employing SIRMS under high pressure has been primarily driven by the search for novel properties and the understanding of structure–property relationships from a spectroscopic viewpoint. Challenges remain, but we may expect progress in the following aspects. In the development of high-pressure experiment stations, we major advances are likely with (i) higher ratios of sample signal to diamond background, (ii) more compact systems, (iii) IR + Raman integration, especially with red laser Raman for ultrahigh pressure measurements (iv) higher spatial resolution, and (v) easier and more rapid alignment for efficient testing.

It is also crucial to extend the current measurement ranges of SIRMS systems. For example, in addition to the low-temperature high-pressure studies that have achieved progress with hydrogen and superconductors, it is desirable to conduct high-temperature high-pressure experiments to investigate correlated electron systems, especially in transition metal oxides. Such experiments will not only provide crucial information on electronic transitions, polaron states, and electron–lattice interactions, but also advance the development of high-temperature high-pressure spectroscopic techniques. For example, with the aim of furthering understanding of charge-ordering phenomena, electron–phonon interactions, and electron–electron interactions, Baldassarre *et al.*[119] studied the metal-to-insulator transition in a V_3O_5 single crystal under a pressure of 10 GPa at room temperature and under ambient pressure at 10–573 K.[119] Although various electronic transitions were observed, a full pressure–temperature phase diagram with regard to electrodynamic behavior is still lacking. Also, high-temperature high-pressure synchrotron-based IR data are useful in helping to understand the evolution of minerals, which is essential for achieving progress in geosciences.

These expected technical developments will hopefully contribute to advances in previously unknown areas, and the results may provide clues to help answer some open questions, such as, is hydrogen really a metal at 427 GPa? Is it possible to measure its spectra? Could we determine the presence of a Drude mode and a bandgap closure from reflectance and absorption measurements, respectively? For high-temperature and even room-temperature superconductors such as metal hydrides, what is the mechanism underlying their pressure-driven superconducting behavior? Is it an electron–phonon mechanism or something else? Is it possible to observe the superconductor gap or to find phonon absorption? For recently emerging functional materials such as hybrid perovskites, is there a general rule for the pressure-driven evolution of the bandgap? If the pressure is high enough, is the final state a metal? What is the role of organic groups in structural evolution, especially for highly disordered phases where XRD cannot provide critical structural information? Full understanding of these various phenomena is likely to be some way off, but the DAC-based SIRMS techniques described here are likely to play a significant role in ultimately obtaining such an understanding.

ACKNOWLEDGMENTS

We thank Dr. Ho-kwang Mao, Dr. Wenge Yang, Dr. Min Chen, Dr. Te Ji, Dr. Huachun Zhu, Dr. Yuzhao Tang, Dr. Xiaojie Zhou, Dr. Jiajia Zhong, Dr. Alexander Goncharov, Dr. Zeming Qi, Dr. Chuansheng Hu, Dr. Federico Gorelli, and Dr. Philip Dalladay-Simpson for their technical support and help. We also thank two anonymous reviewers for their valuable comments on this review article. This work was supported by the NSAF (China) under Grant Nos. U1930401, U2032129, and U2130116.

AUTHOR DECLARATIONS

Conflict of Interest

The authors have no conflict to disclose.

DATA AVAILABILITY

Data sharing is not applicable to this review as no new data were collected.

REFERENCES

[1]P. R. Griffiths and J. A. De Haseth, *Fourier Transform Infrared Spectrometry*, 2nd ed. (John Wiley & Sons Inc, 2006).

[2]H. Okamura, Y. Ikemoto, T. Moriwaki, and T. Nanba, "Infrared spectroscopy techniques for studying the electronic structures of materials under high pressure," Jpn. J. Appl. Phys., Part 1 **56**(5S3), 05FA11 (2017).

[3]R. Bini and G. Pratesi, "High-pressure infrared study of solid methane: Phase diagram up to 30 GPa," Phys. Rev. B **55**(22), 14800–14809 (1997).

[4]X. Xi, C. Ma, Z. Liu, Z. Chen, W. Ku, H. Berger, C. Martin, D. B. Tanner, and G. L. Carr, "Signatures of a pressure-induced topological quantum phase transition in BiTeI," Phys. Rev. Lett. **111**(15), 155701 (2013).

[5]C. Pépin, P. Loubeyre, F. Occelli, and P. Dumas, "Synthesis of lithium polyhydrides above 130 GPa at 300 K," Proc. Natl. Acad. Sci. U. S. A. **112**(25), 7673–7676 (2015).

[6]T. V. Brinzari, K. R. O'Neal, J. L. Manson, J. A. Schlueter, A. P. Litvinchuk, Z. Liu, and J. L. Musfeldt, "Local lattice distortions in $Mn[N(CN)_2]_2$ under pressure," Inorg. Chem. **55**(5), 1956–1961 (2016).

[7]W.-Q. Han, H.-G. Yu, C. Zhi, J. Wang, Z. Liu, T. Sekiguchi, and Y. Bando, "Isotope effect on band gap and radiative transitions properties of boron nitride nanotubes," Nano Lett. **8**(2), 491–494 (2008).

[8]Z. Zhao, H. Zhang, H. Yuan, S. Wang, Y. Lin, Q. Zeng, G. Xu, Z. Liu, G. K. Solanki, K. D. Patel, Y. Cui, H. Y. Hwang, and W. L. Mao, "Pressure induced metallization with absence of structural transition in layered molybdenum diselenide," Nat. Commun. **6**(1), 7312 (2015).

[9]O. Tschauner, S. Huang, E. Greenberg, V. B. Prakapenka, C. Ma, G. R. Rossman, A. H. Shen, D. Zhang, M. Newville, A. Lanzirotti, and K. Tait, "Ice-VII inclusions in diamonds: Evidence for aqueous fluid in Earth's deep mantle," Science **359**(6380), 1136–1139 (2018).

[10]M. Somayazulu, P. Dera, A. F. Goncharov, S. A. Gramsch, P. Liermann, W. Yang, Z. Liu, H.-k. Mao, and R. J. Hemley, "Pressure-induced bonding and compound formation in xenon–hydrogen solids," Nat. Chem. **2**(1), 50–53 (2010).

[11]N. Kong, F. Wan, W. Dai, P. Wu, C. Su, C. Peng, K. Zheng, X. Chen, S. Ling, J. Gong, and Y. Yao, "A cuboid spider silk: Structure-function relationship and polypeptide signature," Macromol. Rapid Commun. **41**(6), 1900583 (2020).

[12]W. Zhang, C. Ye, K. Zheng, J. Zhong, Y. Tang, Y. Fan, M. J. Buehler, S. Ling, and D. L. Kaplan, "Tensan silk-inspired hierarchical fibers for smart textile applications," ACS Nano **12**(7), 6968–6977 (2018).

[13]X. Xi, X.-G. He, F. Guan, Z. Liu, R. D. Zhong, J. A. Schneeloch, T. S. Liu, G. D. Gu, X. Du, Z. Chen, X. G. Hong, W. Ku, and G. L. Carr, "Bulk signatures of pressure-induced band inversion and topological phase transitions in $Pb_{1-x}Sn_xSe$," Phys. Rev. Lett. **113**(9), 096401 (2014).

[14]M. Matsunami, H. Okamura, A. Ochiai, and T. Nanba, "Pressure tuning of an ionic insulator into a heavy electron metal: An infrared study of YbS," Phys. Rev. Lett. **103**(23), 237202 (2009).

[15]A. Dewaele, P. Loubeyre, P. Dumas, and M. Mezouar, "Oxygen impurities reduce the metallization pressure of xenon," Phys. Rev. B **86**(1), 014103 (2012).

[16]A. Irizawa, S. Suga, G. Isoyama, K. Shimai and K. Sato, "Direct observation of a pressure-induced metal-insulator transition in LiV_2O_4 by optical studies," Phys. Rev. B **84**(23), 235116 (2011).

[17]M. J. Rice, "Organic linear conductors as systems for the study of electron-phonon interactions in the organic solid state," Phys. Rev. Lett. **37**(1), 36–39 (1976).

[18]A. B. Kuzmenko, L. Benfatto, E. Cappelluti, I. Crassee, D. van der Marel, P. Blake, K. S. Novoselov, and A. K. Geim, "Gate tunable infrared phonon anomalies in bilayer graphene," Phys. Rev. Lett. **103**(11), 116804 (2009).

[19]M. Dressel and G. Grüner, *Electrodynamics of Solids* (Cambridge University Press, Cambridge, UK, 2002).

[20]G. Burns, in *Solid State Physics* (Academic Press, San Diego, CA, 1985), Chap. 13.

[21]M. Bishop, R. Chellappa, M. Pravica, J. Coe *et al.*, "1,1-diamino-2,2-dinitroethylene under high-pressure-high-temperature," Bull. Am. Phys. Soc. **137**(17), 174304 (2012).

[22]D. Kraemer, M. L. Cowan, A. Paarmann, N. Huse, E. T. J. Nibbering, T. Elsaesser, and R. J. Dwayne Miller, "Temperature dependence of the two-dimensional infrared spectrum of liquid H_2O," Proc. Natl. Acad. Sci. U. S. A. **105**(2), 437–442 (2008).

[23]Y. Yang, Q. Xia, M. Feng, and P. Zhang, "Temperature dependence of IR absorption of OH species in clinopyroxene," Am. Mineral. **95**(10), 1439–1443 (2010).

[24]K. W. Post, B. C. Chapler, L. He, X. Kou, K. L. Wang, and D. N. Basov, "Thickness-dependent bulk electronic properties in Bi_2Se_3 thin films revealed by infrared spectroscopy," Phys. Rev. B **88**(7), 075121 (2013).

[25]G. Firanescu, D. Luckhaus, and R. Signorell, "Size effects in the infrared spectra of NH_3 ice nanoparticles studied by a combined molecular dynamics and vibrational exciton approach," J. Chem. Phys. **125**(14), 144501 (2006).

[26]W. Huang, P.-H. Chien, K. McMillen, S. Patel, J. Tedesco, L. Zeng, S. Mukherjee, B. Wang, Y. Chen, G. Wang, Y. Wang, Y. Gao, M. J. Bedzyk, D. M. DeLongchamp, Y.-Y. Hu, J. E. Medvedeva, T. J. Marks, and A. Facchetti, "Experimental and theoretical evidence for hydrogen doping in polymer solution-processed indium gallium oxide," Proc. Natl. Acad. Sci. U. S. A. **117**(31), 18231–18239 (2020).

[27]P. Dumas, F. Polack, B. Lagarde, O. Chubar, J. L. Giorgetta, and S. Lefrancois, "Synchrotron infrared microscopy at the French Synchrotron Facility SOLEIL," Infrared Phys. Technol. **49**(1–2), 152–160 (2006).

[28]E. Levenson, P. Lerch, and M. C. Martin, "Spatial resolution limits for synchrotron-based spectromicroscopy in the mid- and near-infrared," J. Synchrotron Radiat. **15**(4), 323–328 (2008).

[29]M. C. Martin, U. Schade, P. Lerch, and P. Dumas, "Recent applications and current trends in analytical chemistry using synchrotron-based Fourier-transform infrared microspectroscopy," Trends Anal. Chem. **29**(6), 453–463 (2010).

[30]I. Yousef, L. Ribó, A. Crisol, I. Šics, G. Ellis, T. Ducic, M. Kreuzer, N. Benseny-Cases, M. Quispe, P. Dumas, S. Lefrançois, T. Moreno, G. García, S. Ferrer, J. Nicolas, and M. A. G. Aranda, "MIRAS: The infrared synchrotron radiation beamline at ALBA," Synchrotron Radiat. News **30**(4), 4–6 (2017).

[31]T. Ji, Y. Tong, H. Zhu, Z. Zhang, W. Peng, M. Chen, T. Xiao, and H. Xu, "The status of the first infrared beamline at Shanghai Synchrotron Radiation Facility," Nucl. Instrum. Methods Phys. Res., Sect. A **788**, 116–121 (2015).

[32]G. Liu, L. Kong, W. Yang, and H.-k. Mao, "Pressure engineering of photovoltaic perovskites," Mater. Today **27**, 91–106 (2019).

[33]W. D. Duncan and G. P. Williams, "Infrared synchrotron radiation from electron storage rings," Appl. Opt. **22**(18), 2914–2923 (1983).

[34]R. A. Bosch, "Extraction of edge radiation within a straight section of Aladdin," Rev. Sci. Instrum. **73**(3), 1423–1426 (2002).

[35]Y.-L. Mathis, P. Roy, B. Tremblay, A. Nucara, S. Lupi, P. Calvani, and A. Gerschel, "Magnetic field discontinuity as a new brighter source of infrared synchrotron radiation," Phys. Rev. Lett. **80**(6), 1220–1223 (1998).

[36]P. Dumas, L. M. Miller, and M. J. Tobin, "Challenges in biology and medicine with synchrotron infrared light," Acta Phys. Pol., A **115**(2), 446–454 (2009).

[37]G. L. Carr, O. Chubar, and P. Dumas, in *Spectrochemical Analysis Using Infrared Multichannel Detectors*, edited by R. Bhargava and I. W. Levin (Blackwell Publishing, Oxford, UK, 2006).

[38]C. Hu, X. Wang, Z. Qi, and C. Li, "The new infrared beamline at NSRL," Infrared Phys. Technol. **105**, 103200 (2020).

[39]Bruker Corporation, "Detector characterization using FTIR spectrometer," Application Note AN M161 (2019).

[40]W. R. Mckinney, C. J. Hirschmugl, H. A. Padmore *et al.*, "First infrared beamline at the ALS: Design, construction, and initial commissioning," Proc. SPIE **3153**, 59–67 (1997).

[41]H. Kimura, T. Moriwaki, S. Takahashi *et al.*, "Infrared beamline BL43IR at SPring-8: Design and commissioning," Nucl. Instrum. Methods Phys. Res., Sect. A **467–468**, 441–444 (2001).

[42]S. Kimura, H. Kimura, T. Takahashi, K. Fukui, Y. Kondo, Y. Yoshimatsu, T. Moriwaki, T. Nanba, and T. Ishikawa, "Front end and optics of infrared beamline at SPring-8," Nucl. Instrum. Methods Phys. Res., Sect. A **467–468**, 437–440 (2001).

[43]Y. Ikemoto, T. Moriwaki, T. Hirono, S. Kimura, K. Shinoda, M. Matsunami, N. Nagai, T. Nanba, K. Kobayashi, and H. Kimura, "Infrared microspectroscopy station at BL43IR of SPring-8," Infrared Phys. Technol. **45**(5–6), 369–373 (2004).

[44]R. Pascale, M. Rouzières, Z. M. Qi, and O. Chubar, "The AILES infrared beamline on the third generation Synchrotron Radiation Facility SOLEIL," Infrared Phys. Technol. **49**(1–2), 139–146 (2006).

[45]D. Creagh, J. McKinlay, and P. Dumas, "The design of the infrared beamline at the Australian synchrotron," Vib. Spectrosc. **41**, 213–220 (2006).

[46]D. J. Paterson, J. W. Boldeman, D. D. Cohen, and C. G. Ryan, "Microspectroscopy beamline at the Australian synchrotron," AIP Conf. Proc. **879**(1), 864–867 (2007).

[47]S. Lupi, A. Nucara, A. Perucchi, P. Calvani, M. Ortolani, L. Quaroni, and M. Kiskinova, "Performance of SISSI, the infrared beamline of the ELETTRA storage ring," J. Opt. Soc. Am. B **24**(4), 959–964 (2007).
[48]T. May, T. Ellis, and R. Reininger, "Mid-infrared spectromicroscopy beamline at the Canadian Light Source," Nucl. Instrum. Methods Phys. Res., Sect. A **582**(1), 111–113 (2007).
[49]I. Yousef, S. Lefrançois, T. Moreno, H. Hoorani, F. Makahleh, A. Nadji, and P. Dumas, "Simulation and design of an infrared beamline for SESAME (synchrotron-light for experimental science and applications in the Middle East)," Nucl. Instrum. Methods Phys. Res., Sect. A **673**, 73–81 (2012).
[50]B. Chae, Y. D. Yun, H.-Y. Kim, C. K. Ryu, S. Lefrançois, and P. Dumas, "12D IRS: The infrared synchrotron radiation beamline at PAL," Synchrotron Radiat. News **30**(4), 6–8 (2017).
[51]Z. Zhang, M. Chen, Y. Tong, T. Ji, H. Zhu, W. Peng, M. Zhang, Y. Li, and T. Xiao, "Performance of the infrared microspectroscopy station at SSRF," Infrared Phys. Technol. **67**, 521–525 (2014).
[52]X. J. Zhou, H. C. Zhu, J. J. Zhong, W. W. Peng, T. Ji, Y. C. Lin, Y. Z. Tang, and M. Chen, "New status of the infrared beamlines at SSRF," Nucl. Sci. Tech. **30**(12), 182 (2019).
[53]A. F. Goncharov, L. Kong, and H. K. Mao, "High-pressure integrated synchrotron infrared spectroscopy system at the Shanghai Synchrotron Radiation Facility," Rev. Sci. Instrum. **90**(9), 093905 (2019).
[54]S. Klotz, in *High Pressure Physics*, edited by J. Loveday (CRC Press, Boca Raton, FL, 2012), Chap. 1.
[55]N. Tateiwa and Y. Haga, "Evaluations of pressure-transmitting media for cryogenic experiments with diamond anvil cell," Rev. Sci. Instrum. **80**(12), 123901 (2009).
[56]S. Klotz, K. Takemura, T. Strässle, and T. Hansen, "Freezing of glycerol-water mixtures under pressure," J. Phys.: Condens. Matter **24**(32), 325103 (2012).
[57]C. T. Seagle, W. Zhang, D. L. Heinz, and Z. Liu, "Far-infrared dielectric and vibrational properties of nonstoichiometric wüstite at high pressure," Phys. Rev. B **79**(1), 014104 (2009).
[58]E. Wigner and H. B. Huntington, "On the possibility of a metallic modification of hydrogen," J. Chem. Phys. **3**(12), 764–770 (1935).
[59]E. Babaev, A. Sudbø, and N. W. Ashcroft, "A superconductor to superfluid phase transition in liquid metallic hydrogen," Nature **431**(7009), 666–668 (2004).
[60]S. A. Bonev, E. Schwegler, T. Ogitsu, and G. Galli, "A quantum fluid of metallic hydrogen suggested by first-principles calculations," Nature **431**(7009), 669–672 (2004).
[61]H.-k. Mao and R. J. Hemley, "Ultrahigh-pressure transitions in solid hydrogen," Rev. Mod. Phys. **66**(2), 671–692 (1994).
[62]J. M. McMahon, M. A. Morales, C. Pierleoni, and D. M. Ceperley, "The properties of hydrogen and helium under extreme conditions," Rev. Mod. Phys. **84**(4), 1607–1653 (2012).
[63]H.-K. Mao, X.-J. Chen, Y. Ding, B. Li, and L. Wang, "Solids, liquids, and gases under high pressure," Rev. Mod. Phys. **90**(1), 015007 (2018).
[64]P. Loubeyre, R. Letoullec, and J. P. Pinceaux, "Properties of H_2 under strong compression in a Ne matrix," Phys. Rev. Lett. **67**(23), 3271–3274 (1991).
[65]M. Hanfland, R. J. Hemley, H. K. Mao, and G. P. Williams, "Synchrotron infrared spectroscopy at megabar pressures-vibrational dynamics of hydrogen to 180 GPa," Phys. Rev. Lett. **69**(7), 1129–1132 (1992).
[66]J. H. Eggert, H.-k. Mao, and R. J. Hemley, "Observation of a two-vibron bound-to-unbound transition in solid deuterium at high pressure," Phys. Rev. Lett. **70**(15), 2301–2304 (1993).
[67]S. K. Sharma, H. K. Mao, and P. M. Bell, "Raman measurements of hydrogen in the pressure range 0.2-630 kbar at room temperature," Phys. Rev. Lett. **44**(13), 886–888 (1980).
[68]A. F. Goncharov, J. H. Eggert, I. I. Mazin, R. J. Hemley, and H.-k. Mao, "Raman excitations and orientational ordering in deuterium at high pressure," Phys. Rev. B **54**(22), R15590–R15593 (1996).
[69]C.-s. Zha, Z. Liu, M. Ahart, R. Boehler, and R. J. Hemley, "High-pressure measurements of hydrogen phase IV using synchrotron infrared spectroscopy," Phys. Rev. Lett. **110**(21), 217402 (2013).
[70]C.-s. Zha, H. Liu, J. S. Tse, and R. J. Hemley, "Melting and high P–T transitions of hydrogen up to 300 GPa," Phys. Rev. Lett. **119**(7), 075302 (2017).
[71]R. Pucci, N. H. March, and F. Siringo, "Maximum in vibrational frequency shift of a hydrogen molecule in solid hydrogen under pressure," J. Phys. Chem. Solids **47**(2), 231–236 (1986).
[72]A. F. Goncharov, I. Chuvashova, C. Ji, and H.-k. Mao, "Intermolecular coupling and fluxional behavior of hydrogen in phase IV," Proc. Natl. Acad. Sci. U. S. A. **116**(51), 25512–25515 (2019).
[73]P. Loubeyre, F. Occelli, and P. Dumas, "Hydrogen phase IV revisited via synchrotron infrared measurements in H_2 and D_2 up to 290 GPa at 296 K," Phys. Rev. B **87**(13), 134101 (2013).
[74]M. I. Eremets, A. P. Drozdov, P. P. Kong, and H. Wang, "Semimetallic molecular hydrogen at pressure above 350 GPa," Nat. Phys. **15**(12), 1246–1249 (2019).
[75]N. H. Chen, E. Sterer, and I. F. Silvera, "Extended infrared studies of high pressure hydrogen," Phys. Rev. Lett. **76**(10), 1663–1666 (1996).
[76]C.-S. Zha, Z. Liu, and R. J. Hemley, "Synchrotron infrared measurements of dense hydrogen to 360 GPa," Phys. Rev. Lett. **108**(14), 146402 (2012).
[77]P. Loubeyre, F. Occelli, and P. Dumas, "Synchrotron infrared spectroscopic evidence of the probable transition to metal hydrogen," Nature **577**(7792), 631–635 (2020).
[78]E. Gregoryanz, A. F. Goncharov, R. J. Hemley, H.-k. Mao, M. Somayazulu, and G. Shen, "Raman, infrared, and x-ray evidence for new phases of nitrogen at high pressures and temperatures," Phys. Rev. B **66**(22), 224108 (2002).
[79]R. Bini, L. Ulivi, J. Kreutz, and H. J. Jodl, "High-pressure phases of solid nitrogen by Raman and infrared spectroscopy," J. Chem. Phys. **112**(19), 8522–8529 (2000).
[80]A. F. Goncharov, E. Gregoryanz, H.-k. Mao, Z. Liu, and R. J. Hemley, "Optical evidence for a nonmolecular phase of nitrogen above 150 GPa," Phys. Rev. Lett. **85**(6), 1262–1265 (2000).
[81]A. P. Drozdov, M. I. Eremets, I. A. Troyan, V. Ksenofontov, and S. I. Shylin, "Conventional superconductivity at 203 kelvin at high pressures in the sulfur hydride system," Nature **525**(7567), 73–76 (2015).
[82]A. P. Drozdov, P. P. Kong, V. S. Minkov, S. P. Besedin, M. A. Kuzovnikov, S. Mozaffari, L. Balicas, F. F. Balakirev, D. E. Graf, V. B. Prakapenka, E. Greenberg, D. A. Knyazev, M. Tkacz, and M. I. Eremets, "Superconductivity at 250 K in lanthanum hydride under high pressures," Nature **569**(7757), 528–531 (2019).
[83]E. Snider, N. Dasenbrock-Gammon, R. McBride, M. Debessai, H. Vindana, K. Vencatasamy, K. V. Lawler, A. Salamat, and R. P. Dias, "Room-temperature superconductivity in a carbonaceous sulfur hydride," Nature **586**(7829), 373–377 (2020).
[84]D. Duan, Y. Liu, F. Tian, D. Li, X. Huang, Z. Zhao, H. Yu, B. Liu, W. Tian, and T. Cui, "Pressure-induced metallization of dense $(H_2S)_2H_2$ with high-T_c superconductivity," Sci. Rep. **4**(1), 6968 (2015).
[85]I. Errea, M. Calandra, C. J. Pickard, J. Nelson, R. J. Needs, Y. Li, H. Liu, Y. Zhang, Y. Ma, and F. Mauri, "High-pressure hydrogen sulfide from first principles: A strongly anharmonic phonon-mediated superconductor," Phys. Rev. Lett. **114**(15), 157004 (2015).
[86]N. Bernstein, C. S. Hellberg, M. D. Johannes, I. I. Mazin, and M. J. Mehl, "What superconducts in sulfur hydrides under pressure and why," Phys. Rev. B **91**(6), 060511 (2015).
[87]D. A. Papaconstantopoulos, B. M. Klein, M. J. Mehl, and W. E. Pickett, "Cubic H_3S around 200 GPa: An atomic hydrogen superconductor stabilized by sulfur," Phys. Rev. B **91**(18), 184511 (2015).
[88]J. A. Flores-Livas, A. Sanna, and E. K. U. Gross, "High temperature superconductivity in sulfur and selenium hydrides at high pressure," Eur. Phys. J. B **89**(3), 63 (2016).
[89]F. Capitani, B. Langerome, J.-B. Brubach, P. Roy, A. Drozdov, M. I. Eremets, E. J. Nicol, J. P. Carbotte, and T. Timusk, "Spectroscopic evidence of a new energy scale for superconductivity in H_3S," Nat. Phys. **13**(9), 859–863 (2017).
[90]S. L. James, "Metal-organic frameworks," Chem. Soc. Rev. **32**(5), 276–288 (2003).
[91]H. Furukawa, K. E. Cordova, M. O'Keeffe, and O. M. Yaghi, "The chemistry and applications of metal-organic frameworks," Science **341**(6149), 1230444 (2013).
[92]J. Lee, O. K. Farha, J. Roberts, K. A. Scheidt, S. T. Nguyen, and J. T. Hupp, "Metal–organic framework materials as catalysts," Chem. Soc. Rev. **38**(5), 1450–1459 (2009).
[93]L. E. Kreno, K. Leong, O. K. Farha, M. Allendorf, R. P. Van Duyne, and J. T. Hupp, "Metal–organic framework materials as chemical sensors," Chem. Rev. **112**(2), 1105–1125 (2012).

[94]Y. Cui, Y. Yue, G. Qian, and B. Chen, "Luminescent functional metal–organic frameworks," Chem. Rev. **112**(2), 1126–1162 (2012).
[95]J.-R. Li, R. J. Kuppler, and H.-C. Zhou, "Selective gas adsorption and separation in metal–organic frameworks," Chem. Soc. Rev. **38**(5), 1477–1504 (2009).
[96]L. Zhu and Y.-B. Zhang, "Crystallization of covalent organic frameworks for gas storage applications," Molecules **22**(7), 1149 (2017).
[97]J. Čejka, "Metal-organic frameworks: Applications from catalysis to gas storage. Edited by David Farrusseng," Angew. Chem. **51**(20), 4782–4783 (2012).
[98]Y. Hu, Z. Liu, J. Xu, Y. Huang, and Y. Song, "Evidence of pressure enhanced CO_2 storage in ZIF-8 probed by FTIR spectroscopy," J. Am. Chem. Soc. **135**(25), 9287–9290 (2013).
[99]A. Celeste, A. Paolone, J.-P. Itié, F. Borondics, B. Joseph, O. Grad, G. Blanita, C. Zlotea, and F. Capitani, "Mesoporous metal–organic framework MIL-101 at high pressure," J. Am. Chem. Soc. **142**(35), 15012–15019 (2020).
[100]S. D. Stranks and H. J. Snaith, "Metal-halide perovskites for photovoltaic and light-emitting devices," Nat. Nanotechnol. **10**(5), 391–402 (2015).
[101]C. Yi, J. Luo, S. Meloni, A. Boziki, N. Ashari-Astani, C. Grätzel, S. M. Zakeeruddin, U. Röthlisberger, and M. Grätzel, "Entropic stabilization of mixed A-cation ABX_3 metal halide perovskites for high performance perovskite solar cells," Energy Environ. Sci. **9**(2), 656–662 (2016).
[102]M. R. Filip, G. E. Eperon, H. J. Snaith, and F. Giustino, "Steric engineering of metal-halide perovskites with tunable optical band gaps," Nat. Commun. **5**(1), 5757 (2014).
[103]W. Zhang, G. E. Eperon, and H. J. Snaith, "Metal halide perovskites for energy applications," Nat. Energy **1**(6), 16048 (2016).
[104]G. Liu, L. Kong, J. Gong, W. Yang, H. K. Mao, Q. Hu, Z. Liu, R. D. Schaller, D. Zhang, and T. Xu, "Pressure-induced bandgap optimization in lead-based perovskites with prolonged carrier lifetime and ambient retainability," Adv. Funct. Mater. **27**(3), 1604208 (2017).
[105]G. Liu, L. Kong, P. Guo, C. C. Stoumpos, Q. Hu, Z. Liu, Z. Cai, D. J. Gosztola, H.-k. Mao, M. G. Kanatzidis, and R. D. Schaller, "Two regimes of bandgap red shift and partial ambient retention in pressure-treated two-dimensional perovskites," ACS Energy Lett. **2**(11), 2518–2524 (2017).
[106]G. Liu, J. Gong, L. Kong, R. D. Schaller, Q. Hu, Z. Liu, S. Yan, W. Yang, C. C. Stoumpos, M. G. Kanatzidis, H.-k. Mao, and T. Xu, "Isothermal pressure-derived metastable states in 2D hybrid perovskites showing enduring bandgap narrowing," Proc. Natl. Acad. Sci. U. S. A. **115**(32), 8076–8081 (2018).
[107]L. Kong, G. Liu, J. Gong, L. Mao, M. Chen, Q. Hu, X. Lü, W. Yang, M. G. Kanatzidis, and H.-k. Mao, "Highly tunable properties in pressure-treated two-dimensional Dion–Jacobson perovskites," Proc. Natl. Acad. Sci. U. S. A. **117**(28), 16121–16126 (2020).
[108]L. Kong, G. Liu, J. Gong, Q. Hu, R. D. Schaller, P. Dera, D. Zhang, Z. Liu, W. Yang, K. Zhu, Y. Tang, C. Wang, S.-H. Wei, T. Xu, and H.-k. Mao, "Simultaneous band-gap narrowing and carrier-lifetime prolongation of organic–inorganic trihalide perovskites," Proc. Natl. Acad. Sci. U. S. A. **113**(32), 8910–8915 (2016).
[109]A. Jaffe, Y. Lin, W. L. Mao, and H. I. Karunadasa, "Pressure-induced metallization of the halide perovskite $(CH_3NH_3)PbI_3$," J. Am. Chem. Soc. **139**(12), 4330–4333 (2017).
[110]L. Kong, J. Gong, Q. Hu, F. Capitani, A. Celeste, T. Hattori, A. Sano-Furukawa, N. Li, W. Yang, G. Liu, and H. k. Mao, "Suppressed lattice disorder for large emission enhancement and structural robustness in hybrid lead iodide perovskite discovered by high-pressure isotope effect," Adv. Funct. Mater. **31**(9), 2009131 (2021).
[111]A. Kavner, "Elasticity and strength of hydrous ringwoodite at high pressure," Earth Planet. Sci. Lett. **214**(3–4), 645–654 (2003).
[112]S.-i. Karato, C. Dupas-Bruzek, and D. C. Rubie, "Plastic deformation of silicate spinel under the transition-zone conditions of the Earth's mantle," Nature **395**(6699), 266–269 (1998).
[113]S. Mei and D. L. Kohlstedt, "Influence of water on plastic deformation of olivine aggregates 2. Dislocation creep regime," J. Geophys. Res. **105**, 21471–21481 (2000).
[114]H. P. Scott and Q. Williams, "An infrared spectroscopic study of lawsonite to 20 GPa," Phys. Chem. Miner. **26**, 437–445 (1999).
[115]T. B. Ballaran and R. J. Angel, "Equation of state and high-pressure phase transitions in lawsonite," Eur. J. Mineral. **15**(2), 241–246 (2003).
[116]A. R. Pawley and D. R. Allan, "A high-pressure structural study of lawsonite using angle-dispersive powder-diffraction methods with synchrotron radiation," Mineral. Mag. **65**(1), 41–58 (2001).
[117]B. Schmandt, S. D. Jacobsen, T. W. Becker, Z. Liu, and K. G. Dueker, "Dehydration melting at the top of the lower mantle," Science **344**(6189), 1265–1268 (2014).
[118]M. K. Müller, A. M. Hofmeister, Y. W. Fei, and Z. X. Liu, "High-pressure IR-spectra and the thermodynamic properties of chloritoid," Am. Mineral. **87**, 609–622 (2002).
[119]L. Baldassarre, A. Perucchi, E. Arcangeletti, D. Nicoletti, D. Di Castro, P. Postorino, V. A. Sidorov, and S. Lupi, "Electrodynamics near the metal-to-insulator transition in V_3O_5," Phys. Rev. B **75**(24), 245108 (2007).